NASA/TM—2009-215819

Alloy Design Challenge: Development of Low Density Superalloys for Turbine Blade Applications

Rebecca A. MacKay, Timothy P. Gabb, James L. Smialek, and Michael V. Nathal
Glenn Research Center, Cleveland, Ohio

October 2009

NASA STI Program . . . in Profile

Since its founding, NASA has been dedicated to the advancement of aeronautics and space science. The NASA Scientific and Technical Information (STI) program plays a key part in helping NASA maintain this important role.

The NASA STI Program operates under the auspices of the Agency Chief Information Officer. It collects, organizes, provides for archiving, and disseminates NASA's STI. The NASA STI program provides access to the NASA Aeronautics and Space Database and its public interface, the NASA Technical Reports Server, thus providing one of the largest collections of aeronautical and space science STI in the world. Results are published in both non-NASA channels and by NASA in the NASA STI Report Series, which includes the following report types:

- TECHNICAL PUBLICATION. Reports of completed research or a major significant phase of research that present the results of NASA programs and include extensive data or theoretical analysis. Includes compilations of significant scientific and technical data and information deemed to be of continuing reference value. NASA counterpart of peer-reviewed formal professional papers but has less stringent limitations on manuscript length and extent of graphic presentations.

- TECHNICAL MEMORANDUM. Scientific and technical findings that are preliminary or of specialized interest, e.g., quick release reports, working papers, and bibliographies that contain minimal annotation. Does not contain extensive analysis.

- CONTRACTOR REPORT. Scientific and technical findings by NASA-sponsored contractors and grantees.

- CONFERENCE PUBLICATION. Collected papers from scientific and technical conferences, symposia, seminars, or other meetings sponsored or cosponsored by NASA.

- SPECIAL PUBLICATION. Scientific, technical, or historical information from NASA programs, projects, and missions, often concerned with subjects having substantial public interest.

- TECHNICAL TRANSLATION. English-language translations of foreign scientific and technical material pertinent to NASA's mission.

Specialized services also include creating custom thesauri, building customized databases, organizing and publishing research results.

For more information about the NASA STI program, see the following:

- Access the NASA STI program home page at *http://www.sti.nasa.gov*

- E-mail your question via the Internet to *help@sti.nasa.gov*

- Fax your question to the NASA STI Help Desk at 443–757–5803

- Telephone the NASA STI Help Desk at 443–757–5802

- Write to:
  NASA Center for AeroSpace Information (CASI)
  7115 Standard Drive
  Hanover, MD 21076–1320

NASA/TM—2009-215819

Alloy Design Challenge: Development of Low Density Superalloys for Turbine Blade Applications

Rebecca A. MacKay, Timothy P. Gabb, James L. Smialek, and Michael V. Nathal
Glenn Research Center, Cleveland, Ohio

National Aeronautics and
Space Administration

Glenn Research Center
Cleveland, Ohio 44135

October 2009

Acknowledgments

The authors wish to acknowledge Mr. Henry deGroh, NASA Glenn Research Center (GRC), for alloy density measurements and assistance with vacuum induction melting of screening alloys, Ms. Jami K. Olminsky, formerly of Quality Software Solutions, Inc. (QSS) at GRC, for her diligence in improving the chemical analysis techniques on the ICP, Dr. Anita Garg, University of Toledo, for scanning electron microscopy of the TCP phase, Mr. Michael Cuy, Arctic Slope, for hot salt corrosion testing, and Dr. Ramgopal Darolia, formerly of General Electric Aircraft Engines, for supply of Rene N5 for oxidation and hot corrosion testing.

This work was sponsored by the Fundamental Aeronautics Program at the NASA Glenn Research Center.

Level of Review: This material has been technically reviewed by technical management.

Available from

NASA Center for Aerospace Information
7115 Standard Drive
Hanover, MD 21076–1320

National Technical Information Service
5285 Port Royal Road
Springfield, VA 22161

Available electronically at http://gltrs.grc.nasa.gov

Alloy Design Challenge: Development of Low Density Superalloys for Turbine Blade Applications

Rebecca A. MacKay, Timothy P. Gabb, James L. Smialek, and Michael V. Nathal
National Aeronautics and Space Administration
Glenn Research Center
Cleveland, Ohio 44135

Abstract

New low density single crystal (LDS) alloys have been developed for turbine blade applications, which have the potential for significant improvements in the thrust to weight ratio over current production alloys. An innovative alloying strategy was identified to achieve high temperature creep resistance, alloy density reductions, microstructural stability, and cyclic oxidation resistance. The approach relies on the use of molybdenum (Mo) as a potent solid solution strengthener for the nickel (Ni)-base superalloy; Mo has a density much closer to Ni than other refractory elements, such as rhenium (Re) or tungsten (W). A host of testing and microstructural examinations was conducted on the superalloy single crystals, including creep rupture testing, microstructural stability, cyclic oxidation, and hot corrosion. The paper will provide an overview of the single crystal properties that were generated in this new superalloy design space. The paper will also demonstrate the feasibility of this innovative approach of low density single crystal superalloy design. It will be shown that the best LDS alloy possesses the best attributes of three generations of single crystal alloys: the low density of first-generation single crystal alloys, the excellent oxidation resistance of second-generation single crystal alloys, and a creep strength which exceeds that of second and third generation alloys.

Introduction

The high pressure turbine rotor is subjected to the most demanding conditions in the turbine engine and places a stringent set of requirements on the materials used in that application. The requirements for turbine blades include a balance of creep resistance, temperature capability, environmental resistance, and damage tolerance. Blade performance and durability is achieved through a combination of advanced alloys, sophisticated internal cooling schemes, and thermal barrier coatings. Much has been written over the last 30 years on whether turbine blade alloys have reached their upper limits with respect to creep rupture strength and temperature capability (1, 2). A new approach was envisioned at NASA Glenn Research Center (GRC) wherein the high temperature capability could be achieved in single crystal superalloys with a concurrent decrease in alloy density. The purpose of this paper is to discuss the strategy used to design low density, high creep strength superalloys for turbine blade applications. An overview of mechanical, physical, and environmental properties generated for these innovative superalloys is provided as well.

Turbine blades have been made from nickel (Ni)-base superalloy single crystals for thirty years (3). Alloy strength improvements have in general been achieved by increasing the refractory element content and reducing the chromium (Cr) content. The first generation of single crystal superalloys contained 8-10 wt. % Cr, 4-11 wt. % tungsten (W), and no rhenium (Re). Second generation alloys typically contained 5-8 wt. % Cr, 5-8 wt. % W, and 3 wt. % Re and have attained successful application in commercial and military aircraft engines. Third generation alloys were designed to increase the temperature capability and creep resistance further by raising the Re levels up to 6 wt. % and lowering the Cr level to the 2-4 wt. % range.

Turbine airfoil alloy development culminated in the development of fourth generation single crystal alloys, such as EPM102 (4-6). These alloys are among the strongest nickel-base superalloy single crystals developed to date. EPM102 was co-developed by General Electric, Pratt & Whitney, and GRC in NASA's High Speed Research Program of the late 1990's (4, 6). Although originally intended for use in the High Speed Civil Transport, the alloy is more likely to see first service in military applications. Fourth generation alloys contain high levels of refractory metals (Re, W, and tantalum (Ta)) and low Cr levels, similar to those in the third generation alloys. However, fourth generation alloys distinguish themselves with the addition of ruthenium (Ru). EPM102 has exceptional creep strength, but has a high density of 9.2 g/cm^3, compared to 9.0 g/cm^3 for third generation and 8.64 to 8.95 g/cm^3 for second generation, and 7.9 to 8.7 g/cm^3 for first generation alloys (7-9). Figure 1 (6-8, 10-18) illustrates the trend in single crystal superalloy development wherein higher creep strength capability has historically been achieved with corresponding increases in alloy density, as a result of increasingly higher amounts of refractory metal additions in the design of the alloy.

Besides creating higher alloy densities, the use of increasingly higher amounts of refractory elements has pushed third and fourth generation alloys toward microstructural instability. The phase instabilities observed after high temperature exposures in some of the third and fourth generation alloys include topologically close packed (TCP) phases and secondary reaction zone (SRZ) (4-8, 19). The TCP phase is rich in refractory elements and is a discrete precipitate usually taking the form of a lath, needle, or plate. Although a small amount of TCP phase is tolerable, excessive quantities of TCP within the bulk of the superalloy are believed to decrease the creep rupture strength, especially long-term properties, by reducing the amount of refractory elements in solution in the gamma matrix (7, 9, 20, 21). In contrast, SRZ is a three-phase instability with TCP and stringers of gamma contained within a gamma prime matrix. Although a similar feature (i.e., cellular colonies) may sometimes be observed along grain boundaries or in dendrite cores in internal regions of superalloys rich in refractory metals, SRZ was first observed in the superalloy just beneath the diffusion zone of aluminide bondcoats (19). SRZ is believed to severely decrease the mechanical properties (4, 5) by reducing the load-bearing cross-section of the superalloy.

For the last 25 years, numerous attempts to progress beyond superalloys by considering alternatives such as ceramics and intermetallics have been largely unsuccessful, because the required balance of properties has not been achieved with these alternative candidates. Figure 2 is a schematic which illustrates the balance of properties needed for turbine engine applications and that which is attained by three classes of materials; ceramics are shown in red, intermetallics are in green, and superalloys are in blue in the figure. The figure indicates that toughness is a property that is sacrificed in ceramics and intermetallics with concurrent increases in temperature capability. Although ceramics possess excellent creep and oxidation resistance, their temperature advantage is smaller than expected because of the high level of cooling achieved in the superalloy/TBC system. When the cooling requirements of ceramics are considered along with their very poor toughness and resistance to foreign object damage, it appears that a substantial time frame is still required for the development of ceramics, especially for high pressure turbine applications.

Thus, metallic systems are still needed for the high pressure turbine engine. A very worthwhile goal is to achieve further improvements in the thrust to weight ratio by reducing the density of a new alloy compared to current production (second generation) alloys, Rene N5, SC180, and PWA 1484. A reduction in the turbine blade weight has a cascading effect throughout the entire rotor (disk, hub, and shaft) and to non-rotating support structures, traditionally achieving a total engine weight savings of 8 to 10 times the blade weight savings (22). This blade weight savings and the total engine weight savings are quite substantial because up to 100 turbine blades may be set on a turbine disk, with a number of disks per engine, and a number of engines per aircraft. Thus, because of the potential for significant impact in weight savings, a task was undertaken at GRC to develop low density single crystal alloys for turbine blade applications.

Alloy Design Strategy

An alloying strategy was identified to achieve high temperature creep resistance, alloy density reductions, microstructural stability, and cyclic oxidation resistance. The approach used in this alloy development effort was based upon research conducted on single crystal alloys at GRC in the 1980's (23, 24), although originally developed under Air Force sponsorship of the Rapid Solidified Processing Program (25, 26). These nickel-base alloys were simple quaternary compositions that were rich in refractory metal, namely molybdenum (Mo). Mo is a potent solid solution strengthener, but has a density much closer to Ni than other refractory elements, such as Re and W. The strongest alloys (24) in this quaternary series actually had creep strengths slightly exceeding those of the third generation alloy, CMSX-10, which demonstrates the potential of this alloy design strategy. Despite its significant creep strength and its low density of ~8.4 g/cm^3, the quaternary alloy required significant compositional modifications to attain the desired balance of properties for turbine rotor applications. Thus, the challenge was to retain its exceptional creep strength and low density, while improving other desirable properties such as oxidation resistance.

A Design of Experiments (DoE) approach was employed using RS/1® software by Brooks Automation, Inc. The DoE minimized the number of alloys to be cast, while enabling good predictive capability of properties. This DoE approach required a selection of alloying elements and their ranges. The baseline alloy selected in this design strategy was based on the quaternary compositions mentioned above and contained 6.1 wt. % aluminum (Al), 12 wt. % Mo, 6.2 wt. % Ta, and a balance of Ni. Specific elements were identified as being likely candidates for improving the balance of properties of the baseline alloy, and these elements included yttrium (Y), Cr, Re, and cobalt (Co). Y was added for improved oxidation resistance, because it was believed to enhance the adherence of the protective oxide scales (27-29). Retained Y levels were targeted in the range between 50 to 100 ppmw. The remaining element levels were chosen so that the resultant matrix of alloys would likely contain a range of creep strength, oxidation resistance, and alloy stability from stable to very unstable. This range would allow for good predictive capabilities within the compositional design space, and optimization experiments could be performed to achieve targeted property levels in subsequent casting rounds. Based on earlier work (24), it was expected that alloys would be stable if their combined Mo+Re+Cr contents were less than 14 wt. %, although the presence of Co was expected to shift this limit to higher levels. Cr was added to the alloy base for improved oxidation resistance; Cr contents were aimed between 0 and 5 wt. %. Re was added because of its well known effect of strengthening the gamma matrix and reducing gamma prime coarsening, and levels of up to 3 wt. % Re were included. It was desirable to avoid using Ru in these alloys, since it is considered an unconventional and expensive alloying element. Instead, Co was chosen as an alloying element since it is a more conventional elemental addition for superalloys and is believed to improve alloy stability in a manner similar to that of Ru (4, 6). The Co levels ranged from 0 to 10 wt. %. With all of these compositional changes made to the baseline quaternary alloy, the Mo level would also need to be optimized. The Mo level was varied from 7 to 12 wt. %, and it is this high Mo range, in conjunction with reactive elements such as Y and with relatively low Cr, that makes this alloy design truly unique (30).

A computer-aided, D-optimal design methodology (31, 32) was adopted to model the four element (Cr, Co, Mo, and Re) variables and all their two-way interactions. This method allowed initial inclusion of alloys mandated by engineering judgment and then employed an algorithm which tested all possible alloys within the design space. The algorithm then selected a minimum number of alloys within the design space which minimized the joint confidence intervals of all estimated coefficients. It was determined that a set of twelve alloys would enable all main and interaction effects to be estimated with no substantial cross correlations.

The low density superalloys (LDS) chosen for study in the DoE are given in Table I. The alloy name refers to the level of each element variable. For example, LDS-0000 refers to the low content end of each element range (0 Cr, 0 Co, 7 Mo, and 0 Re, all in wt. %), and LDS-1111 would refer to the high level of each element (5 Cr, 10 Co, 12 Mo, and 3 Re, all in wt. %). A 5 in the alloy name refers to the mid-level of the element (2.5 Cr, 5 Co, 9.5 Mo, and 1.5 Re, all in wt. %). Three alloys were mandated in this DoE: the baseline (LDS-0010) alloy, the centerpoint (LDS-5555) alloy in the design space, and an "engineering judgment" alloy (LDS-5051) which was an initial estimate of a favorable composition for strength and stability. In LDS-5051, despite its nomenclature, the Mo content was intentionally decreased from the mid-level of 9.5 wt. % to 9.0 wt. %, in order to improve expected stability.

A preliminary round of twelve alloys was cast at GRC in polycrystalline form by vacuum induction melting (VIM). This casting method provided an inexpensive way to obtain initial screening data and guidance for the subsequent, and more expensive, single crystal casting rounds. Density, microstructural stability, and cyclic oxidation were measured in these polycrystalline alloys. Polycrystalline VIM castings provided reasonably reliable data that assisted in the downselection of alloys for casting into single crystal form. The biggest inconsistency in behavior between the polycrystalline and single crystal castings was with respect to the scale phases and specific weight changes that developed for the VIM castings during cyclic oxidation. The reason for this inconsistency may be attributed either to a lack of homogeneous retention of reactive elements (Y) in the polycrystalline material or to trace or tramp elements picked up during VIM processing. Despite this, the ranking of the alloys with respect to oxidation resistance was similar between polycrystalline and single crystal versions. Use of the VIM castings provided beneficial screening of preliminary alloys for a variety of measured properties, but single crystals were necessary for firm conclusions on the effects of composition on mechanical and environmental properties.

Statistical models were developed subsequently to help downselect a subset of seven alloys for casting in single crystal form at a commercial vendor. The subset of single crystal alloys that was procured is also indicated in the right-most column in Table I. A host of testing and microstructural examinations was conducted on the single crystals, including creep rupture testing, microstructural stability, cyclic oxidation, and hot corrosion. The remainder of this paper will provide an overview of the single crystal properties that were generated in this new superalloy design space. Furthermore, the paper will demonstrate the feasibility of this innovative approach of low density single crystal superalloy design. It will be shown that the best LDS alloy possesses the best attributes of three generations of single crystal alloys: the low density of first-generation single crystal alloys, the excellent oxidation resistance of second-generation single crystal alloys, and the creep strength which exceeds that of second and third generation alloys.

Materials and Experimental Procedures

Seven LDS alloys were cast into single crystal slabs at a commercial casting vendor. Small quantities of carbon (C) and boron (B) were added as grain boundary strengthening elements, which has been done more recently in third and fourth generation alloy, in order to deal with undesirable grain boundary defects (4, 9) that may be present. The slab castings measured approximately 15 cm long in the single crystal growth direction, 5 cm wide, and 0.6 cm thick. Single crystal castings were batch solutioned at a commercial heat treatment vendor; a few castings of LDS-1110 were left in the as-cast condition for subsequent solution treatment cycles since lower maximum temperatures were anticipated for that alloy. The furnace chamber of the batch heat treatment was evacuated twice and then backfilled with 400 microns of argon before ramping in steps to a maximum temperature of 1315°C which was held for 6 hours. The load was fan quenched in argon to temperatures below 1093°C at a rate of 43°C/min. The slabs were chemically etched and electrolytically etched at the commercial vendor to reveal grain defects,

and Laue X-ray diffraction was performed on each slab to determine primary crystallographic orientation. Density measurements were performed using the Archimedes method (33) of water displacement.

Bulk chemical analyses were performed at GRC by inductively coupled plasma emission spectroscopy (ICP) at the top and bottom sections of at least one casting of each composition. Because of its effect on oxide scale adhesion, sulfur (S) content and other trace or tramp elements were also analyzed on selected LDS alloys by Glow Discharge Mass Spectroscopy (GDMS) at SHIVA Technologies. Pins, nominally 1.6 mm square by 19 mm long, were supplied for this analysis.

Prior to machining creep rupture specimens, sections of the 0.6 cm-thick single crystal slabs were given a simulated coating cycle plus age in a gas quench furnace at GRC, because turbine blades are typically coated before service. This simulated coating cycle plus age was conducted in argon at 1079°C for 4 hours, then argon gas quenched to below 871°C, and aged at 871°C for 12 hours. Creep rupture specimens were then machined by slow speed grinding. The threaded creep specimens had a nominal 3.175 mm gage diameter, 1.9 cm gage length, and an overall length of 6.8 cm. Creep testing was performed in air according to ASTM-E 139-06 (34) at temperatures ranging from 816 to 1093°C, with the majority of testing at 982 and 1093°C. Creep extensometers were attached to V-notches that were ground into specimen shoulders, and temperatures were maintained to within ± 2°C along the specimen gage length.

To determine the microstructural stability of the alloys, samples were sectioned from the solutioned single crystal slabs and aged in argon at 982°C and 1093°C for 200 and 500 hr. All samples were water quenched to ambient temperature at the end of the aging treatment. The aged samples were metallographically prepared and examined in the unetched condition by back-scattered scanning electron (BSE) microscopy. Images were taken at five locations at 100X, 250X and 500X for measurement of the area fraction of TCP precipitates by quantitative image analysis software. Carbide area fractions were also measured in the as-solutioned condition by this same technique. Electron dispersive spectroscopy (EDS), as well as phase extraction (35) and X-ray diffraction, were utilized for third phase identification.

Cyclic oxidation testing was performed at GRC on coupons that were nominally 1.3 cm square by 0.25 cm thick. Oxidation coupons were polished on all surfaces to a 600 grit finish, then weighed, cleaned, and re-weighed. Cyclic oxidation tests were performed in a furnace in air at 1100°C for 200 cycles. Each cycle consisted of a one-hour hold at 1100°C followed by a 10-minute cool. At numerous intervals throughout the oxidation tests, weight changes were measured, and samples were visually examined for scale phases and general scale adherence. All samples were given a moisture sensitivity test by breath spallation after 100 and 200 cycles to help determine scale adherence or lack thereof. The oxide scales that developed were analyzed after 200 cycles of testing by X-ray diffraction. Cyclic oxidation tests were also performed on Rene 80, first-generation single crystal alloy Rene N4, and second-generation single crystal alloy Rene N5 for comparison to the LDS alloys. Selected alloys were also tested in cyclic oxidation at 1150°C for 200 cycles.

Hot salt corrosion testing was conducted in a 0.3 Mach burner rig at GRC on pins having an 11.5 cm length and a 0.63 cm diameter. The pins were machined from LDS alloys and from a series of commercial single crystal superalloy baselines. Eighteen pins were loaded into a carousel for testing. The test conditions included a one-hour heating cycle to 900°C followed by a 5 to 10 minute cooling cycle; 2 ppm sea salt was applied during the full heating cycle at a solution injection rate of 3.33 ml/min. All alloys were tested through a minimum of 100 cycles, and selected alloys were tested through 200 cycles. Weight measurements, visual inspections, and photos were obtained at least every 10 cycles during the first 100 cycles and every 20 cycles thereafter. Maximum pin diameters were obtained with calipers every 40 to 60 cycles.

Results and Discussion

Chemical Analyses

The analyzed chemistries of the LDS single crystal slab castings shown in Table II are averages of the ICP measurements obtained from the top and bottom sections of the 15 cm long slabs. The variation in the analyzed contents of the main elements from top to bottom of the castings was typically less than 0.1 wt. %, with no obvious trends as a function of location within the slab. The mean analyzed chemistries were within 0.3 wt. % of the aims for each main element, but more typically within 0.1 wt. % of the aims. Thus, there was no particular difficulty in obtaining the aim chemistry targets for these unique single crystal alloy compositions.

The analyzed levels of the interstitial elements, B, C, nitrogen (N), and oxygen (O), were also all within acceptable limits. B and C were intentionally added at very low levels. B may combine with Cr or Mo to form borides which reside at grain boundaries (9), and C may combine with Ta or Mo to form carbides. Borides and carbides can precipitate on undesirable grain boundaries that sometimes form in single crystals, and adding these interstitial elements in very small quantities has become a fairly standard practice in advanced single crystal alloys.

No aim target for S was specified for the single crystal castings, since Y was intentionally added to the alloy design because of its well-known effect to getter the S. The S content and other trace and tramp elements were analyzed on selected LDS alloys by Glow Discharge Mass Spectroscopy (GDMS) at SHIVA Technologies. The analyzed S contents are given in Table II. S was typically measured to be 3 ppmw in these LDS alloys. Considerable effort has been expended by superalloy manufacturers to reduce the S in superalloy melts to levels below 10-20 ppmw (9), and the LDS alloys have S contents nearly an order of magnitude lower than this limit.

The retained Y content was observed to vary significantly from top to bottom of the single crystal castings. Although Y is used to getter sulfur in the alloys, Y is a reactive element that can also react with the common shell molds used to cast superalloys, so obtaining the targeted level of retained Y can sometimes be a challenge. Figure 3 shows the levels of Y measured in the top and bottom sections, respectively, of two different slab castings labeled “B” and “D” for all seven single crystal alloys. It is evident in the figure that the top sections of the LDS single crystal castings consistently possessed Y levels around the desired minimum of about 50 ppmw. However, the bottom sections of the slabs were usually enriched in Y at levels significantly above the desired maximum of 100 ppmw. The enrichment in Y was observed to have caused a small amount (<0.6 vol. %) of incipient melting during solutioning in the bottom casting sections, as evidenced by the Y-rich precipitates and their associated pores present in low quantities in the bottom sections. Less than 1 vol. % of incipient melting is generally considered acceptable by industry standards. Nevertheless in this study, only the top halves of each slab were used for physical, mechanical, and environmental property testing. Thus, the retained Y levels ranged from 50 to 100 ppmw in all of the single crystal material used for the testing discussed in this paper.

Density Measurements

The measured densities for the LDS design space are plotted in green in Figure 4 and are compared to densities of various single crystal alloys (ref. 8, 9, 36) from first through fourth generations. The lowest density measured in LDS space was that for LDS-1000 and the highest was for LDS-0111. These alloys have the lowest and highest combined levels, respectively, of Mo and Re. It is noteworthy that the majority of the LDS alloys had densities less than that of first-generation alloy, Rene N4, and all LDS alloys had densities less than second-generation alloys CMSX-4, SC180, and PWA1484. The markedly

lower alloy densities of the LDS alloys is the result of the use of a high level of Mo as a strengthening element, the low level of Re, the absence of W, the useful range of Co, and the lower Ta content. Thus, the alloy design was a success with regard to decreasing density relative to that of commercial alloys used in production of single crystal turbine blades.

A regression analysis was performed for the measured densities and the analyzed chemistries of the elements that were varied. Stepwise forward and reverse selection of significant terms were compared, with at least 90% probability of significance necessary for inclusion of a term. The regression analysis indicated that the terms for Cr, Mo, and Re, as well as the term for a CrMo interaction, were significant. Both Re and Mo increased alloy density, while Cr reduced it. Not surprisingly, Re had the strongest effect on density, and Co had no significant effect on alloy density. These single element regression results were consistent with each individual element's density relative to that of Ni. A CrMo interaction term was statistically significant and improved the equation fit; however, the effect of this interaction was weaker than the linear effects of Cr and Mo. The physical basis of the CrMo interaction term is unclear.

The density data are displayed graphically in Figure 5, where the densities predicted from the regression model are plotted as a function of the measured densities for each alloy. Very good agreement is shown in the figure between the alloy densities predicted by the LDS density predictions and the measured alloy densities. The LDS regression model provided a very good fit with a correlation coefficient adjusted for the number of estimated coefficients (R^2 adj.) of 99.1%. Predictions using JMatPro® 4.0, a commercially available software program that utilizes a commercial Ni alloy database, are also shown for comparison. This software tool did a fairly good job of predicting the alloy densities in this study with an R^2 adj. of 94.4%. The solid blue line in the figure has a slope of 1.0, which also demonstrates graphically that the LDS regression more closely predicted the measured density values, as compared to the JMatPro® predictions.

Creep Rupture

Creep rupture testing of the LDS single crystals was conducted at 982 and 1038°C at GRC. Most alloys were tested at two stresses at each temperature. Figure 6a shows a bar chart of the creep rupture life data for all of the alloys. LDS-1101, LDS-5555, and LDS-5051 were consistently the strongest alloys overall. LDS-1101 had the longest creep rupture lives at 982°C at both applied stress levels, whereas LDS-5555 was stronger at 1093°C at the lower stress level of 110 MPa. LDS-1101, LDS-5555, and LDS-5051 had equivalent lives at 1093°C and 124 MPa. The remaining alloys were considerably weaker in creep, except for LDS-0010 at 1093°C and 110 MPa. Similar alloy trends were observed for time to 1% creep strain and time to 2% creep strain, as seen in Figures 6b and c, respectively. Having lower strength alloys in this group of seven alloys was not unexpected. LDS-1000 and LDS-0101 had low refractory metal contents, so lower creep lives were anticipated for these alloys. On the other hand, LDS-1110 had a very high refractory metal content and was observed to be highly unstable with respect to TCP phases in the alloy, which would explain the weakness of the alloy. Part of the alloy design strategy was to ensure that a range of properties was obtained. In this way, the composition space would be sufficiently covered so that creep rupture properties could be optimized within that space.

Typical creep curves are shown in Figures 7a and b for the strongest LDS alloys at 982 and 1093°C, respectively. The 982°C creep curves of LDS-1101 show an incubation period at both stresses, followed by a gradually increasing creep rate through tertiary creep. The 1093°C creep curves of LDS-5555 exhibit primary creep with a rapid transition into a prolonged steady-state creep regime followed by a sharp transition into tertiary creep. Despite the primary creep regime at 1093°C, the time to 1% creep strain was a large fraction of the rupture life. Differences in the shapes of the creep curves have been associated with different creep mechanisms related to the rafting kinetics of the gamma prime phase.

Less well defined steady-state creep regimes at 982°C, similar to that in Figure 7a, have been associated with slower rafting kinetics in 3 wt. % Re alloys (37).

The creep strengths of different alloys are often compared using a Larson Miller Parameter (LMP) plot, which enables direct comparison between alloys that were creep tested under different conditions. With the LMP curves generated for two different alloys, a creep life advantage can be calculated for a given temperature and stress; or alternatively, as is often done for turbine blade materials, a temperature advantage can be calculated for one material over another at a given life and applied stress.

A series of LMP plots in Figures 8 through 10 demonstrate several advantages of the three strongest low density alloys, LDS-1101, LDS-5555, and LDS-5051 over second, third, and fourth generation superalloy single crystals. Figure 8 shows that LDS-1101 has higher creep rupture strengths than Rene N5, since the LMP curve for LDS-1101 lies to the right of that for Rene N5 (7) at all stress levels. Furthermore, LDS-1101 has a very significant 22 to 40°C temperature advantage over second generation Rene N5 for a wide range of applied stresses. The biggest improvement observed for LDS-1101 was at the lower applied stress levels used during creep testing at 1093°C. LDS-5555 and LDS-5051 had creep strengths similar to those of Rene N5 at the high stress levels, but had significant temperature advantages over Rene N5 at the lower stress levels. Since these three LDS alloys also have slightly lower densities than Rene N5 (Figure 4), the temperature advantage of the LDS alloys would be increased further if the applied stress was corrected for density.

Favorable comparisons to third and fourth generation alloys have also been demonstrated. Figure 9 shows the creep strength of the LDS alloys relative to third generation alloys Rene N6 (7) and CMSX-10 (38) and to fourth generation EPM102 (4, 6). Although there is significant overlap in the LMP curves for these alloys, there are a few differences evident. At stress levels of 210 MPa and above, Rene N6 has more favorable creep strength relative to the LDS alloys. Above 170 MPa, EPM102 and CMSX-10 have improved creep strengths over the LDS alloys and Rene N6. However, below 170 MPa, the creep data for all of these alloys converge, and the LDS alloys have rupture strengths that are more comparable to these third and fourth generation alloys. The densities of the LDS alloys are 6 to 7% lower than EPM 102 and 5 to 6% lower than CMSX-10. Thus when alloy density is taken into account, the LDS alloys have normalized creep strengths that are very similar to fourth generation EPM102 over a wide range of stresses, Figure 10. Furthermore, the LDS alloys exceed the density compensated creep strength of CMSX-10 in the low stress range and provide up to a 20°C temperature advantage over CMSX-10. Thus, the LDS alloys provide their greatest potential benefits at the low stress/high temperature creep conditions. Coupling these creep property advantages with a density reduction has the potential of providing fuel efficiency and a significant impact in the overall vehicle system weight. A reduction in the density of rotating parts results in an 8 to 10X multiplier in total engine weight savings (22), which translates into reduced fuel consumption and reduced emissions.

Microstructural Stability

The microstructure of each LDS alloy was examined in the as-solutioned condition by scanning electron microscopy. Except for LDS-1110, all single crystal alloys had a maximum solution temperature of 1315°C for 6 hr. LDS-1110 was heat treated at 1288°C to reduce its incipient melting to < 1 vol. %. Four alloys with the higher Mo contents (LDS-5051, LDS-5555, LDS-0010, and LDS-1110) contained blocky, Mo and Ni-rich carbides in the residual interdendritic areas of the as-solutioned condition, Figure 11a. X-ray diffraction indicated that these carbides were M_6C (39). The volume fraction of carbides in these alloys was obtained by taking BSE images of five different areas at 100X and then measuring the area fraction of the carbides using a quantitative image analysis. Area fraction was considered a good estimate of the volume fraction because the distribution of third phases in the material is similar through the depth of material. These higher Mo content alloys typically contained about 0.6 vol. % of carbide in the as-

solutioned condition, except for LDS-1110, which contained about 1.3 vol. % carbide. The three alloys with lower Mo levels (LDS-1101, LDS-1000, and LDS-0101) contained no appreciable amounts of carbides (<0.04 vol. %) in the as-solutioned condition, Figure 11b, despite the C addition that was made to each alloy.

To determine the microstructural stability of the LDS alloys at elevated temperatures, samples were aged isothermally at 982 and 1093°C in argon for 200 and 500 hr. TCP laths precipitated in some of the aged alloys. Figure 12 shows microstructures after 500 hr of aging at 982°C for LDS-5051 and LDS-1101. In LDS-5051, carbides are primarily evident at 100X, Figure 12a. Higher magnifications were necessary to resolve the fine-scale TCP laths in LDS-5051, Figure 12b, which precipitated on certain crystallographic planes. LDS-1101 had no significant carbide content in the as-solutioned condition, but a low volume fraction of TCP phase is slightly discernable after 500 hr of aging at 100X, Figure 12c. The TCP lath morphology in LDS-1101 is more evident at 500X, Figure 12d; the laths in LDS-1101 are thicker and shorter in appearance than those in LDS-5051. Significantly smaller quantities of TCP phase are present in LDS-1101 (Figure 12d), compared to that for LDS-5051 (Figure 12b) after the same aging exposure. EDS indicated that the TCP laths contain high levels of Mo, Ni, and Re and a low level of Cr. Ta was not detected in the TCP phase. X-ray diffraction identified the TCP phases as sigma in LDS-5051 and as mu in LDS-1110 (39); the details of this phase identification will be reported in a subsequent publication.

Figures 13a and b show that the TCP phase morphologies observed after aging at 1093°C were similar to those seen at 982°C. Again, LDS-5051 had a fairly high volume fraction of long, fine-scale TCP laths, whereas the TCP laths in LDS-1101 tended to be fewer in number, thicker, and shorter in length. However, the TCP volume fraction in LDS-5051 appeared to be slightly reduced at the higher temperature. In addition to the isothermally aged samples, the TCP phase in longitudinal sections of creep tested specimens was also examined. Figures 13c and d show the microstructures in LDS-5051 and LDS-1101, respectively, that developed during creep testing at 1093°C. The TCP phase morphologies and quantities after creep testing appeared similar to those after isothermal aging, and thus were used to supplement stability data from isothermally aged samples.

Area fractions of the TCP phase were measured in all LDS alloys after aging or after creep rupture testing. The TCP phase quantities obtained are displayed in Figures 14a and b as a function of exposure time at 982 and 1093°C, respectively. The data points represent the means of five different images from each specimen, and the error bars represent the 95% confidence intervals. Data from the isothermally aged samples are shown at either 200 or 500 hr, and exposure times other than these precise durations represent the rupture lives of the creep tested samples that were examined for TCP phases. Figures 14a and b illustrate that two alloys precipitated significant quantities of TCP phase, but the remaining five alloys had TCP phase contents that were < 1 vol. % at either temperature.

Alloys with ≤1 vol. % TCP phase content are generally considered to be stable alloys, and these alloys included LDS-1101, LDS-5555, LDS-0010, LDS-0101, and LDS-1000. In fact, LDS-0010, LDS-0101, and LDS-1000 precipitated no TCP phase after extended exposure times at either 982 or 1093°C. LDS - 1101 and LDS-5555 precipitated small quantities of TCP phase up to 0.6 vol. % at either temperature. The equilibrium volume fractions of TCP phase may not have been reached in these latter two alloys, since the third phase contents appear to be increasing at a very low linear rate, except for LDS-1101 at 1093°C, where the equilibrium amount of TCP phase may have been reached by 200 hr. It is interesting to note that LDS-1101 and LDS-5555 were the two strongest LDS alloys in creep in this round of cast alloys. Although there are a number of other factors that affect creep properties besides microstructural stability, it appears that LDS-1101 and LDS-5555 have acceptable TCP phase stability limits for exceptional creep strength.

In contrast, two of the alloys (LDS-5051 and LDS-1110) exhibited more significant instabilities with TCP phase contents between 2 and 9 vol. % at 982 and 1093°C, Figure 14. There was significantly more scatter in the TCP volume fraction measurements for these unstable alloys, as evidenced by their large error bars. Comparison of Figures 14a and b also indicates that more TCP phase precipitated in LDS-5051 and LDS-1110 at 982°C than at 1093°C. Both of these alloys appeared to have reached their equilibrium TCP phase content during exposure at 982°C, since their 95% confidence intervals overlapped after 25 hr for LDS-1110 and by 200 hr for LDS-5051. At 1093°C, LDS-1110 reached its equilibrium TCP phase content within the first 40 hr of high temperature exposure. However, the kinetics for TCP phase precipitation were considerably slower at 1093°C for LDS-5051, and its TCP phase content appeared to be increasing linearly through 500 hr of exposure. It is interesting to note that LDS-5051 was one of the more creep resistant alloys in this round of alloys, despite its relatively high TCP phase content. This may suggest that the creep resistance of single crystal alloys may be more tolerant of the presence of TCP phase than previously thought, although the impact of TCP laths on fatigue properties also needs to be examined.

The qualitative trends in TCP phase formation as a function of composition were not unexpected. It is well known that increasing the refractory metal content increases the propensity for TCP formation. This is consistent with the EDS analysis performed in this study on extracted TCP residue, which showed that the TCP laths are rich in Mo, Re, Ni, and to a lesser extent, Cr. However, the key to the alloy development process is to know with very high accuracy the critical concentration limits of the key strengthening elements and for the combination of elements. A simple, yet useful, representation of alloying effects on TCP phase formation is to plot the volume fraction of TCP phase against the total refractory metal content (Cr + Mo + Re). This is shown in Figures 15a and b for the TCP volume fraction measured after 500 hr of aging at 982 and 1093°C, respectively. Both plots show the same features, namely that most of the alloys were stable, and there appeared to be a critical refractory metal content of about 15 wt. %, above which TCP phase precipitation was induced. There was an intermediate range between ~14 - 15 wt. % where both stable (LDS-1101) and unstable (LDS-5051) alloys exist. In fact, LDS-5051 had more TCP phase than LDS-1101, despite its lower refractory metal content. Other factors in addition to the total refractory metal content are known to be important in determining stability, including the partitioning of elements between gamma and gamma prime, the individual character of each elements, plus the presence or absence of other elements. For example, Re is expected to be more important to TCP phase formation compared to Mo, because of its potency as well as its stronger partitioning to gamma. Finally, the presence or absence of Co has been found to affect stability, apparently by influencing the solubility limits for refractory elements in the gamma and gamma prime (4, 16). The higher Co content of LDS-1101 could be a major reason why it is more stable than the Co-free LDS-5051.

Several methods have been developed to predict more accurately the TCP phase precipitation in complex alloys. These include the PHACOMP method (40), which calculates a critical electron vacancy value, Nv3b, for the gamma phase in a given alloy, and the newer d-electrons concept (41), which calculates a different critical value Md. Both of these methods predict TCP phase instability when the alloy content exceeds a critical value. These calculations were also conducted on the current LDS alloys, but the alternative methods did not improve upon the simple refractory metal content approach displayed in Figure 15. In particular, neither of these methods was able to explain the relative stability ranking of LDS-5051 and LDS-1101. In addition, the commercial software package JMatPro® 4.0 was also used to predict stability of these experimental alloys; however serious discrepancies between the model and experiments were found. In a future report, the use of multiple regression analysis to produce a more accurate prediction of stability will be presented.

Cyclic Oxidation

Cyclic oxidation tests were performed on coupons in air at 1100 and 1150°C for 200 cycles. All of the LDS alloys contained 50 ppmw Y, which was added specifically to enhance cyclic oxidation resistance by gettering S and improving oxide scale adherence. The LDS alloys also contained 6.0 wt. % Al, which was in the same range as that in the most oxidation resistant single crystal alloys. In general, Cr was the element with the design space that was the most influential variable to the oxidation behavior. The discussion below was therefore organized by considering groups of alloys with similar Cr levels.

The cyclic oxidation curves generated during furnace cycling at 1100°C are shown in Figure 16 for the LDS alloys and selected commercial single crystal alloys. Figure 16a displays the cyclic oxidation data for the 5 wt. % Cr alloys (LDS-1000, LDS-1101, and LDS-1110) and the commercial alloy Rene N5. The figure shows that the LDS alloys with 5 wt. % Cr exhibited small positive weight gains of less than 0.4 mg/cm^2 through 200 cycles. Furthermore, the LDS alloys had a cyclic oxidation response which appeared very similar to that of the highly oxidation-resistant Rene N5 throughout the 200 cycle test. Small positive weight gains during testing are considered beneficial because this suggests that adherent, protective scales are developing on the test coupons. However, weight losses during testing denote detrimental behavior indicative of scale spallation, which can expose bare metal.

Coupon surfaces were visually examined at frequent intervals during 1100°C testing for overall scale appearance. The cyclic oxidation sample of LDS-1000 developed a uniform, light gray interference tint after 1 cycle, Figure 17a. After 200 cycles, gray oxides dominated the surface appearance of the LDS-1000 coupon, and blue oxides were present in some local spots, primarily at sample edges, Figure 17b. These oxide colors are characteristic of a protective alumina healing layer and spinel transients, respectively. The other alloys containing 5 wt. % Cr also tended to form adherent alumina layers and spinel transients. Figure 17c shows LDS-1101 with adherent gray and a few blue oxides after 200 cycles. Coverage of the protective alumina layer on another 5 wt. % alloy, LDS-1110, appeared slightly less uniform than that of LDS-1000 and LDS-1101.

Figure 16b compares the 1100°C cyclic oxidation data for a representative 5 wt. % Cr LDS alloy (LDS-1000), the 2.5 wt. % Cr alloys (LDS-5051 and LDS-5555), and the Cr-free alloys (LDS-0101 and LDS-0010). First generation single crystal alloy Rene N4, and Rene 80 are also displayed in the figure for comparison. It is evident in the figure that only the 5 wt. % Cr alloy exhibited small positive weight gains throughout the 200 cycle test. All other alloys displayed in the figure underwent rapid initial weight gains and then rapid weight losses, the magnitudes of which appeared correlated to the Cr level in the LDS alloys. For example, the 2.5 wt. % Cr-containing alloys, LDS-5051 and LDS-5555, both exhibited rapid initial weight gains of about 1 mg/cm^2 followed by early weight losses and then relatively little weight change after 50 cycles, Figure 16b. This was likely an initial growth and spallation transient followed by a form of rapid healing. The macro photos of the coupon surface in Figure 18 for LDS-5555 supported this mechanism. LDS-5555, with its low Cr content, developed a rumpled scale that spalled with light brushing after the completion of 1 cycle (Figures 18a and b). Samples were brushed when there was some history or indication that the scales were largely detached, thereby giving an erroneous weight indication. The specks left behind after spallation of oxide scale (Figure 18b), were fewer in number after 200 cycles, since some of these areas appeared healed by the blue oxide scale (Figure 18c). Overall, the behavior of LDS-5555 and LDS-5051 in cyclic oxidation was more similar to that of Rene N4, and thus a level of only 2.5 wt. % Cr appeared insufficient to provide optimal oxidation resistance for this alloy design space. These results were not particularly surprising since increased Cr content in superalloys has been weakly correlated with improved cyclic oxidation resistance, although this typically occurs at levels higher than 5 wt. % (27).

The cyclic oxidation behavior at 1100°C for the Cr-free LDS alloys (LDS-0010 and LDS-0101) is also displayed in Figure 16b. These LDS alloys exhibited large initial weight gains of up to 3 mg/cm^2, followed by sharp drops in specific weight change, and then significantly decreased rates of weight loss. This behavior was similar to that of the 2.5 wt. % Cr LDS alloys, except that the magnitudes of these initial weight changes in the Cr-free alloys were more precipitous. Figure 16b shows that the Cr-free LDS alloys had oxidation behaviors worse than that of Rene N4 but better than Rene 80, which had a steady and continuous weight loss of -281 mg/cm^2 by 200 cycles and showed no form of healing. The poor overall performance of these alloys is the result of formation of NiO as the primary scale and appreciably higher initial growth rates coupled with proportionally more scale spallation. For example, after 1 cycle, LDS-0010 initially developed a thick, non-adherent green oxide (Figure 19a) typical of NiO. This scale exhibited massive spallation after the coupon surface was brushed upon completion of 1 cycle, Figure 19b. After 200 cycles, LDS-0010 developed blue and gray oxides characteristic of spinel and alumina healing layers, Figure 19c, although the blue scales were more predominant. The other Cr-free alloy (LDS-0101) was observed to form a gray oxide initially that spalled after brushing the coupon surface, and glossy gray and blue scales with varying degrees of adherence were evident after 200 cycles, Figure 20.

The phases in the oxide scales were identified by X-ray diffraction scans after the completion of 200 cycles of cyclic oxidation testing at 1100°C. Table III lists the major scale phases that were present, and a qualitative indication of the strength (strong, medium, or weak) of the XRD peaks for each phase is given in the table. Alumina (α-Al_2O_3) was identified as a prominent primary scale phase only in the 5 wt. % Cr alloys, and was present, at most, as a minor phase in the 0 and 2.5 wt. % Cr alloys. However, spinel [$(Ni,Co)(Al,Cr)_2O_4$ with a_o=8.060 to 8.114 Å] and rutile were prominent in the scales on all the LDS alloys. NiO was present to varying degrees but appeared to be strongest in the oxide scales of alloys in which no alumina phase was detected (i.e., LDS-0101 and LDS-5555). Presumably, rutile, spinel, and NiO reflect rapid transient oxidation for alloys that are borderline alumina formers, until a healing Al_2O_3 layer is set up at the oxide-metal interface. The rutile $CrTaO_4$/$NiTa_2O_6$ phase is commonly observed on superalloys and may be playing a role in preventing excessive and persistent NiO growth. Careful examination of oxide-substrate cross-sections and surface microstructures are needed to fully understand the roles of the various phases that are present in these oxide scales. Nonetheless, the LDS alloys that were strong alumina formers (LDS-1000, LDS-1101, and LDS-1110) were observed to have improved cyclic oxidation performance at 1100°C.

Selected alloys (LDS-1101, LDS-5051, and Rene N5) were also tested in cyclic oxidation at 1150°C, and these results are shown in Figure 21. LDS-1101 also exhibited small, positive weight gains at 1150°C, and looked promising relative to Rene N5 up to 200 cycles. It should be noted that the Rene N5 data at 1150°C was generated in another cyclic oxidation run presented in Reference 42. LDS-5051 exhibited similar initial weight gains at 1150°C and 1100°C, but its rate of subsequent weight loss at 1150°C was higher than that at 1100°C. Additional coupons of these LDS alloys were given a hydrogen (H_2) anneal by placing them in a furnace with flowing H_2 at 1250°C for 50 hr prior to cyclic oxidation. H_2 annealing has been shown (43) to getter sulfur in superalloys. Figure 21 shows that oxidation-resistant LDS-1101 was not improved by the H_2 anneal, although LDS-5051 was improved substantially during the first 100 cycles with a prior H_2 anneal. In addition, moisture-laden, breath spallation tests were performed on both LDS alloys at 100 and 200 cycles. Any vertical drop in specific weight change observed at 100 and 200 cycles in Figure 21 was the result of the breath spallation test, which caused some oxide to spall to bare metal, particularly for LDS-5051. LDS-1101 with the prior H_2 anneal exhibited a very small weight change at 200 cycles due breath spallation. Larger spallation events at 100 and 200 cycles were exhibited by LDS-5051 in both the as-received and H_2 annealed conditions. It has been shown that moisture dramatically increases scale spallation rates, although it has little effect on scale growth rates (44-48). Coupons of Rene N5 with 53 ppmw Y and without Y were also tested in cyclic oxidation (42, 44) at 1150°C. Figure 21 shows that the behavior of Rene N5 without Y was somewhat similar to that of LDS-

5051 with Y, and the addition of 53 ppmw Y to Rene N5 improved its behavior tremendously, making it similar to that of LDS-1101. Thus, it appears that H_2 annealing provides no further improvements in an LDS alloy with adequate Cr, Al, and Y levels, whereas in a low (2.5 wt. %) Cr alloy, hydrogen annealing improves the oxidation resistance beyond the capacity of Y.

Based on the tests, Mo levels between 7 and 12 wt. % and Re levels up to 3 wt. % are tolerable with respect to cyclic oxidation in the presence of 5 wt. % Cr. Mo is generally thought to be particularly detrimental to oxidation resistance. Thus, it is remarkable that an alloy, such as LDS-1101, with 4.7 wt. % Cr, 6.0 wt. % Al, 50 ppmw Y, and 7.1 wt. % Mo has a cyclic oxidation behavior very similar to that of second generation alloy Rene N5, which is well known to possess excellent oxidation resistance. Furthermore, these results indicate that a Cr level near 5 wt. % is crucial in this alloy design for optimal cyclic oxidation resistance. Increasing the Cr content to still higher levels might provide further improvements in the cyclic oxidation resistance for these alloys. However, Cr levels higher than 5 wt. % are expected to compromise the creep rupture strength, so a trade-off in properties is likely. The effect of Co is not straightforward, as it appears to be neutral or beneficial; future regression modeling may help in this regard to pinpoint this and other compositional effects.

Hot Salt Corrosion

Cyclic hot salt corrosion testing was conducted in a Mach 0.3 burner rig on the LDS alloys and a series of commercial single crystal superalloys. Test conditions included a one-hour heating cycle to 900^{o}C followed by a 5 to 10 minute cooling cycle; 2 ppm sea salt was applied during the full heating cycle. All samples were tested through 100 cycles, and most alloys were tested through 200 cycles. Figure 22a shows the cyclic hot corrosion weight change data on an enlarged scale for LDS-1101, several commercial alloys (Rene N5, CMSX-4, and CMSX-10), and fourth generation single crystal alloy EPM102. With exception of EPM102, these alloys all followed the same trends with small weight gains during the first 50 cycles and very small, gradual weight losses over the next 150 cycles. The same small perturbations in the curves were observed between these commercial alloys and LDS-1101 which may reflect some subtle change during testing in an uncontrolled, but variable, rig parameter such as salt deposition rate, salt dispersion, or coking. Nonetheless, these alloys in Figure 22a appeared to provide good, or at least acceptable, hot corrosion resistance for nickel-base superalloy single crystals with relatively low levels of Cr. Superalloys with Cr contents of 15 wt. % or greater are found to be highly corrosion-resistant, and chromia-forming alloys are preferred in corrosive conditions over alumina-forming alloys (9).

The hot corrosion weight change data in Figure 22b are shown for all of the LDS alloys and Rene N5 through 200 cycles. A range of behavior is evident in the figure. LDS-1101 and Rene N5 are represented in the figure by nearly horizontal lines as these alloys exhibited a minimal weight gain of 6-9 mg. The remainder of the LDS alloys exhibited substantial weight changes of 50-180 mg after the completion of 200 cycles. The 12 wt. % Mo alloys (LDS-0010 and LDS-1110) were stopped at 100 cycles because of excessive corrosion. LDS-5051 and LDS-5555 with 9 and 9.5 wt. % Mo, respectively, also did not perform well in hot corrosion. Mo has long been associated with poor hot corrosion resistance (9), which makes the good hot corrosion resistance of LDS-1101 with 7 wt. % Mo even more surprising, though other more severe conditions have not been tested. LDS-1000 had high corrosion rates despite its Mo and Cr levels, which were equivalent to that of LDS-1101. Duplicate samples of LDS-1000 were tested to verify the poor hot corrosion behavior of LDS-1000, since this was one of the most oxidation-resistant LDS alloys along with LDS-1101. Apparently, main element and/or subtle interaction effects between Cr, Co, Mo, and Re in hot corrosion do not apply to oxidation resistance; it is expected that future regression modeling will help to sort out these effects.

The macro photo in Figure 23a shows the hot corrosion pins after 100 cycles, and the approximate burner rig flame impingement area is superimposed on the figure. The "U" and "L" in the figure represent the approximate upper and lower extremes, respectively, of the flame impingement area. LDS-1101 and the commercial alloy (Rene N5, CMSX-4, and CMSX-10) pins remained cylindrical with a minor amount of discoloration in the flame impingement area. The photo also shows that when excessive corrosion was apparent on other alloys the pins exhibited a barrel shape in the impingement area with flaking corrosion product. Barrel patterns are correlated to those pins having the massive weight gains. Higher magnification in Figure 23b shows cracks extending internally into the alloy. The zone of maximum corrosion was not located at the centerline axis ("CL" in the figure) of the burner rig nozzle, but rather at the lower edge of the heated area. This may be due to the sea salt being injected in the lower half of the burner.

One issue with using weight change as an indicator of hot corrosion resistance is that some of the weight gain measured is due to deposition of salt product on the alloy pin rather than due entirely to hot corrosion reactions and scale formation. Likewise, some of the weight loss may be due to flaking off of the built-up salt deposit and not due to spallation of corrosion reaction products. Leaching of two samples indicated that up to about 10 mg can be ascribed to the existing salt product condensed on the entire sample pin. As a result, the weight change measurement is not necessarily reflective of the hot corrosion resistance of the alloy. Weight change is used as an indicator of hot corrosion resistance, however, since it is one of the most straightforward measurements to obtain without destructive examination of the pins. Clearly, some metallographic cross-sections are needed for examination of inner and outer layers, in order to verify the true hot corrosion behavior.

Maximum pin diameter measurements were also obtained using calipers on the corrosion pins at the lower end, "L," of the flame impingement area. These diameters were obtained parallel to the flow of the burner flame. The diameter measurements are shown in Figure 22c and appeared largely correlated with the weight change measurements since those alloys with the highest weight change exhibited the largest diametral growth. LDS-1101 was the most corrosion resistant of the LDS alloys tested in this study and showed very little change in diameter over the first 200 cycles. LDS-1101 did exhibit the beginning of a small corrosion nodule after 200 cycles. Other LDS alloys showed considerable diameter thickening, whereas Rene N5 showed essentially no diameter change. It should be noted that salt buildup occurred on the cooler sample areas that did not exhibit corrosion; hence, although the salt deposit may have affected weight changes, it did not affect pin diameter measurements which were taken from the hot sample area at position L in Figure 23b. Future analysis of cyclic hot corrosion testing of these alloys will include detailed chemical analyses of soluble deposits by ICP, X-ray diffraction of surface products, and microscopy of surface and internal layers. Additional testing through 500 cycles will also be pursued for promising alloys to determine if these alloy trends continue.

Concluding Remarks and Future Work

This paper has summarized the physical, mechanical, and environmental properties of the new low density single crystal alloys, and has demonstrated the feasibility of the alloy design strategy. This series of Ni-base single crystal superalloys, with relatively high Mo as a refractory metal addition, provides a range of responses in physical, mechanical, and environmental properties, which is considered beneficial for future optimizations. But can the required balance of properties be attained in a single alloy? Clearly, the density goal was achieved over a majority of the alloy design space investigated, and Figure 4 illustrates the significant density savings achieved by this alloy design, relative to second, third, and fourth generation single crystals. However, oxidation resistance, hot corrosion resistance, and creep resistance are more challenging to achieve in one conceptual alloy.

The oxidation resistance of the LDS alloys with 5 wt. % Cr (LDS-1101, LDS-1000, and LDS-1110) was very promising and compared very favorably with Rene N5 in furnace cycling tests up to 200 cycles at 1100°C. Burner rig oxidation tests provide a more realistic environment for turbine engine applications, however cyclic oxidation in furnaces has been a cost effective and highly reliable tool for screening. Nevertheless, burner rig oxidation tests are planned for the near future, along with longer term furnace cycling tests.

The Mach 0.3 burner rig hot salt corrosion tests indicated good hot corrosion resistance for LDS-1101 based on weight changes through 200 cycles, but the performance of the other 5 wt. % Cr alloys (LDS-1000 and LDS-1110) was surprisingly not as good. Detailed characterization of the corrosion products may be required to verify and fully explain the corrosion behavior. It appears that 5 wt. % Cr is needed but is not sufficient for hot corrosion resistance.

Creep rupture testing demonstrates that LDS-1101, LDS-5555, and LDS-5051 have up to a 40°C improvement over second generation Rene N5, and properties mid-way between third generation CMSX-10 and fourth generation EPM102 in the low stress regime. When a density correction is made, these three LDS alloys surpass CMSX-10 during 1093°C creep. Of the three LDS alloys, LDS-1101 possesses the best 982°C creep properties, LDS-5555 possesses the best 1093°C creep properties, and LDS-5051 remains close in third place. It is interesting to note that the LDS alloys with no TCP phase precipitation were all weak in creep rupture. LDS-1101 and LDS-5555 both precipitated minor amounts of TCP ($\leq$ l vol. %), and were consistently the best LDS alloys in creep. LDS-5051 was fairly strong in creep, despite its precipitation of up to 6 vol. % TCP. Thus, a true upper limit to an allowable amount of TCP phase has not yet been determined for this design space. Alloys with TCP phase contents greater than 1 vol. % may be permissible without a significant drop in creep strength, although its effect on fatigue needs to be investigated.

Based on all of these experimental results, LDS-1101 clearly has the best balance of properties with respect to oxidation, creep, hot corrosion, and density. Optimization studies have begun within LDS compositional space, centering around the composition of LDS-1101. Tweaks to the Mo level, Mo /Re trades, and variations in the Co level were made to see their effects on TCP phase formation tendencies, creep rupture properties, and environmental properties. This optimization round of alloys has been cast, and testing is in progress. Combining all the alloy data together should provide a clearer picture of allowable TCP phase levels and its true impact on mechanical properties. Regression models will be developed and compared to available software packages for predicting superalloy behavior.

Conclusions

1. The challenge for co-optimizing stability, creep resistance, density, and cyclic oxidation in this unique superalloy design space has been achieved. LDS-1101 with 5 wt. % Cr, 10 wt. % Co, 7 wt. % Mo, and 3 wt. % Re has the best balance of properties and brings together the best attributes of three generations of single crystal alloys with a:
    a. creep strength exceeding that of third generation single crystal alloys in low applied stress conditions;
    b. oxidation resistance approaching that of the most oxidation-resistant second-generation alloy (a gold-standard in the industry); and
    c. low density of the first-generation single crystal alloys.

2. The alloy design was a success because a range of properties was achieved, thereby enabling predictive models to be developed and optimization studies to be conducted in the future. This could

become critically important for tailoring compositions for specific applications where a different balance of properties is desired or where a slight boost in a specific property may be needed.

3. The most creep resistant alloys in the design space had low to medium Mo levels, medium to high Cr levels, and medium to high Re levels. Co contents for the most creep resistant alloys ranged over the full spectrum examined in this study.

4. The most creep resistant alloys had TCP phase contents that were less than 0.6 vol. %. However, LDS-5051 (with 2.5 wt. % Cr, 0 wt. % Co, 9.5 wt. % Mo, and 3 wt. % Re) was also creep resistant and precipitated up to 6.0 vol. % TCP phase. This may suggest that single crystal alloys may be more tolerant of TCP phases during creep rupture than previously thought, although the impact of TCP laths on fatigue properties also needs to be examined.

5. The 5 wt. % Cr LDS alloys (LDS-1101, LDS-1000, and LDS-1110) were alumina formers and exhibited oxidation behaviors like those of the most oxidation-resistant, second-generation single crystal alloys. Surprisingly, oxidation resistant alloys were achieved in LDS alloys with Mo levels as high as 12 wt. %.

6. LDS-1101 exhibited similar hot corrosion behavior to that of several commercial alloys (Rene N5, CMSX-4, and CMSX-10), based on weight changes through the first 200 cycles in a Mach 0.3 burner rig at 900°C. The good performance of LDS-1101 was unexpected, because Mo had long been associated with poor hot corrosion resistance. It also appears that 5 wt. % Cr is needed, but is not sufficient, for hot corrosion resistance in this design space.

References

1. R. F. Decker, "Superalloys - Does Life Renew at 50?," in Superalloys 1980, J. K. Tien, S. T. Wlodek, H. Morrow III, M. Gell, and G. E. Maurer, eds., American Society for Metals, Metals Park, OH, (1980), pp. 1-20.
2. H. Harada and H. Murakami, "Design of Ni-Base Superalloys," in Computational Materials Design, T. Saito, ed., Springer, Berlin (1999), vol. 34, p. 40.
3. M. Gell, D. N. Duhl, and A. F. Giamei, "The Development of Single Crystal Superalloy Turbine Blades," in Superalloys 1980, J. K. Tien, S. T. Wlodek, H. Morrow III, M. Gell, and G. E. Maurer, eds., American Society for Metals, Metals Park, OH, (1980), p. 205-214.
4. Enabling Propulsion Materials Program: Final Technical Report, Volume 4, Task J - Long-Life Turbine Airfoil Materials System, 01 October 1998 to 31 October 1999, NASA Contract NAS 3-26385, May 2000.
5. R. A. MacKay, A. Garg, F. J. Ritzert, and I. E. Locci, "Assessment of Creep Capability of HSR-EPM Turbine Airfoil Alloys," originally published internally as NASA Technical Memorandum UEET001, February 2001, later as NASA/TM—2007-214921.
6. S. Walston, A. Cetel, R. MacKay, K. O'Hara, D. Duhl, and R. Dreshfield, "Joint Development of a Fourth Generation Single Crystal Superalloy," in Superalloys 2004, K. A. Green, T. M. Pollock, H. Harada, T. E. Hawson, R. C. Reed, J. J. Schirra, and S. Watson, eds., TMS, Warrendale, PA, 2004, p. 15. Also in NASA/TM-2004-213062.
7. W. S. Walston, K. S. O'Hara, E. W. Ross, T. M. Pollock, and W. H. Murphy, "René N6: Third Generation Single Crystal Superalloys, " in Superalloys 1996, R. D. Kissinger D.J. Deye, D.L. Anton, A.D. Cetel, M.V. Nathal, T.M. Pollock, and D.A. Woodford, eds., TMS, Warrendale, PA, 1996, pp. 27-34.

8. G. L. Erickson, "The Development and Application of CMSX® -10," in Superalloys 1996, R. D. Kissinger, D. J. Deye, D. L. Anton, A. D. Cetel, M. V. Nathal, T. M. Pollock, and D. A.Woodford, eds., TMS, Warrendale, PA, 1996, pp.35-44.
9. R. C. Reed, The Superalloys: Fundamentals and Applications, Cambridge University Press, Cambridge, 2006, p. 148-170.
10. D. A. Ford and R. P. Arthey, "Development of Single Crystal Alloys for Specific Engine Applications," in Superalloys 1984, M. Gell, C. S. Kortovich, R. H. Bricknell, W. B. Kent, and J. F. Radavich, eds., TMS, Warrendale, PA, 1984, p. 115.
11. K. Harris, G. L. Erickson, and R. E. Schwer, "Mar-M 247 Derivations – CM 247 LC DS Alloy CMSX Single Crystal Alloys Properties & Performance" in Superalloys 1984, M. Gell, C. S. Kortovich, R. H. Bricknell, W. B. Kent, and J. F. Radavich, eds., TMS, Warrendale, PA, 1984, p. 221.
12. A.D. Cetel, and D. N. Duhl, "Second-Generation Nickel-Base Single Crystal Superalloy," in Superalloys 1988, D. N. Duhl, G. Maurer, S. Antolovich, C. Lund, and S. Reichman, eds., TMS, Warrendale, PA, 1988, p. 235.
13. K. Harris, G. L. Erickson, S. L. Sikkenga, W. D. Brentnall, J. M. Aurrecoechea, and K. G. Kubarych, "Development of the Rhenium Containing Superalloys CMSX-4® & CM 186 LC® for Single Crystal Blade and Directionally Solidified Vane Applications in Advanced Turbine Engines," in Superalloys 1992, S. D. Antolovich, R. W. Stusrud, R. A. MacKay, D. L. Anton, T. Khan, R. D. Kissinger, and D. L. Klarstrom, eds., TMS, Warrendale, PA, 1992, p. 297.
14. E. W. Ross and K. S. O'Hara, "Rene N4: A First Generation Single Crystal Turbine Airfoil Alloy with Improved Oxidation Resistance Low Angle Boundary Strength and Superior Long Time Rupture Strength," in Superalloys 1996, R. D. Kissinger, D. J. Deye, D. L. Anton, A. D. Cetel, M. V. Nathal, T. M. Pollock, and D. A. Woodford, eds., TMS, Warrendale, PA, 1996, p. 1.
15. G. L. Erickson, "The Development of the CMSX® -11B and CMSX® -11C Alloys for Industrial Gas Turbine Application," in Superalloys 1996, R.D. Kissinger, D. J. Deye, D. L. Anton, A. D. Cetel, M. V. Nathal, T. M. Pollock, and D. A. Woodford, eds., TMS, Warrendale, PA, 1996, p. 45.
16. P. Caron, "High γ' Solvus New Generation Nickel-Based Superalloys for Single Crystal Turbine Blade Applications," in Superalloys 2000, T. M. Pollock, R. D. Kissinger, R. R. Bowman, K. A. Green, M. McLean, S. Olson, and J. J. Schirra, eds., TMS, Warrendale, PA, 2000, p. 737.
17. Y. Koizumi, T. Kobayashi, T. Yokokawa, J. Zhang, M. Osawa, H. Harada, Y. Aoki, and M. Arai, "Development of Next-Generation Ni-Base Single Crystal Superalloys," in Superalloys 2004, K. A. Green, T. M. Pollock, H. Harada, T. E. Hawson, R. C. Reed, J. J. Schirra, and S. Watson, eds., TMS, Warrendale, PA, 2004, p. 35.
18. X. Nguyen-Dinh, US patent 4935072, 1990.
19. W. S. Walston, J. C. Schaeffer, and W. H. Murphy, " A New Type of Microstructural Instability in Superalloys – SRZ," in Superalloys 1996, R.D. Kissinger, D. J. Deye, D. L. Anton, A. D. Cetel, M. V. Nathal, T. M. Pollock, and D. A. Woodford, eds., TMS, Warrendale, PA, 1996, pp. 9-18.
20. D. N. Duhl, "Alloy Phase Stability Requirements in Single Crystal Superalloys," in Alloy Phase Stability and Design, G. M. Stocks, D. P. Pope, and A. F. Giamei, eds., MRS, Pittsburgh, PA, (1991), vol. 186, pp. 389-400.
21. W. S. Walston, "Microstructural Stability of Advanced Single Crystal Superalloys," in Long Term Stability of High Temperature Materials, G. E. Fuchs, K. A. Dannemann, and T. C. Deragon, eds., The Minerals, Metals & Materials Society (1999), p. 43-53.
22. Personal communication with Dr. Hugh R. Gray, NASA Glenn Research Center, Sept. 2001.
23. R. A. MacKay and L. J. Ebert, "Factors Which Influence Directional Coarsening of Gamma Prime During Creep in Nickel-Base Superalloy Single Crystals," in Superalloys 1984, M. Gell, C. S. Kortovich, R. H. Bricknell, W. B. Kent, and J. F. Radavich, eds., TMS, Warrendale, PA, 1984, pp. 135-144.

24. R. A. MacKay, M. V. Nathal, and D. D. Pearson, "Influence of Molybdenum on the Creep Properties of Nickel-Base Superalloy Single Crystals," Metall. Trans. A, vol. 21A, 1990, pp. 381-388.
25. A. Cox , et al., DARPA Contract F33615-76-C-5136, (1979).
26. P. L. Martin, H. A. Lipsitt, and J. C. Williams, "The Structure of As-Extruded RSR Ni-Al-Mo and Ni-Al-Mo-X Alloys," Proc. Second Int'l. Conf. on Rapid Solidification Processing, Reston, VA, 24-26 March 1980, pp. 123-128.
27. J. L. Smialek, C. A. Barrett, and J. C. Schaeffer, "Design for Oxidation Resistance," in ASM Handbook: Materials Selection and Design, vol. 20, 1997, pp. 589-602.
28. J. L. Smialek and R. Browning, "Current Viewpoints on Oxide Adherence Mechanisms," in Electrochemical Society Symposium Proceedings on High Temperature Materials Chemistry III, 1986, pp. 259-271.
29. J. G. Smeggil, A. W. Funkenbusch, and N. S. Bornstein, Metall. Trans. A, vol. 17A, 1986, pp. 923-932.
30. R. A. MacKay, T. P. Gabb, J. L. Smialek, and M. V. Nathal, U. S. Patent 7,261,783 B1, 2007.
31. G. E. P. Bach and N. R. Draper, "Empirical Model-Building and Response Surfaces," Wiley Publishers, 1987, pp. 489-501.
32. F. J. Ritzert, D. Arenas, D. Keller, and V. Vasudevan, "The Effect of Alloying a Topologically Close Packed Phase Instability in Advanced Nickel-Base Superalloy Rene N6," NASA TM-1998-206622, Washington, D.C., May 1998.
33. Mettler Density Determination Kit ME-40290, Mettler Instrument Corporation, Hightstown, NJ, 1981, pp. 1-5.
34. ASTM Designation: E139-06, "Standard Test Methods for Conducting Creep, Creep-Rupture, and Stress-Rupture Tests of Metallic Materials," pp. 319-331, Volume 3.01 Metals – Mechanical Testing: Elevated and Low-Temperature Tests: Metallography, 2006 Annual Book of ASTM Standards, ASTM International, West Conshokocken, PA, 2006.
35. M. J. Donachie, Jr., and O. H. Kriege, J. Mat., 1972, vol. 7, no. 3, pp. 269-278.
36. EPM Program: Annual Technical Progress report, Volume 3, Task C – Other Critical Components, 1 January 1993 – 31 December 1993, NASA Contract NAS3-26385, January 1994.
37. A. Ma, D. Dye, and R. C. Reed, Acta Materiala, 56, 2008, pp. 1657-1670.
38. G. L. Erickson, U. S. Patent 5,366,695, 1994.
39. R. A. MacKay, R. Rogers, and A. Garg, unpublished research, March 2008.
40. S. T. Wlodek, "The Stability of Superalloys," in Long Term Stability of High Temperature Materials, G. E. Fuchs, K. A. Dannemann, and T. C. Deragon, eds., TMS, 1999, p. 18.
41. M. Moringa, N. Yukawa, H. Adachi, and H. Ezaki, "New PHACOMP and its Applications to Alloys Design, in Superalloys 1984, M. Gell, C. S. Kortovich, R. H. Bricknell, W. B. Kent, and J. F. Radavich, eds., TMS, Warrendale, PA, 1984, p. 523.
42. J. L. Smialek and B. A. Pint, "Optimizing Scale Adhesion on Single Crystal Superalloys," NASA/TM-2000-210362, August 2000.
43. J. L. Smialek and B. K. Tubbs: "Effect of Sulfur Removal on Scale Adhesion to PWA 1480," Metallurgical and Materials Transactions, 26A, 1995, pp. 427-435.
44. J. L. Smialek and G. N. Morscher, "Delayed Alumina Scale Spallation on Rene N5+Y: Moisture Effects and Acoustic Emission," Mat. Sci. Eng. A332, 2002, pp. 11-24.
45. R. Janakiramanan, G. H. Meier, and F. S. Pettit, Met.Trans., 30A, 1999, pp. 2905-2913.
46. M. C. Maris-Sida, G. H. Meier, and F. S. Pettit, Met. Trans., 34A, 2003, pp. 2609-2619
47. B. A. Pint, J. A. Haynes, Y. Zhang, K. L. More, and I. G. Wright, Surf. Coat. Tech., 201, 2006, pp. 3852-3856.
48. C. Zhou, J. Yu, S. Gong, and H. Xu, Materials Science and Engineering A348, 2003, pp. 327-332.

Table I
Alloy Design (in weight percent)

Alloy	Al	Cr	Co	Mo	Re	Ta	Y (ppmw)	Ni	PX Casting	SX Casting
LDS-0000	6.1	0	0	7	0	6.2	50-100	80.70	✓	
LDS-0010 (baseline)	6.1	0	0	12	0	6.2	50-100	75.70	✓	✓
LDS-0101	6.1	0	10	7	3	6.2	50-100	67.70	✓	✓
LDS-0110	6.1	0	10	12	0	6.2	50-100	65.70	✓	
LDS-0111	6.1	0	10	12	3	6.2	50-100	62.70	✓	
LDS-5051	6.1	2.5	0	9	3	6.2	50-100	73.20	✓	✓
LDS-5555 (center)	6.1	2.5	5	9.5	1.5	6.2	50-100	69.20	✓	✓
LDS-1000	6.1	5	0	7	0	6.2	50-100	75.70	✓	✓
LDS-1011	6.1	5	0	12	3	6.2	50-100	67.70	✓	
LDS-1100	6.1	5	10	7	0	6.2	50-100	65.70	✓	
LDS-1101	6.1	5	10	7	3	6.2	50-100	62.70	✓	✓
LDS-1110	6.1	5	10	12	0	6.2	50-100	60.70	✓	✓

PX = polycrystal
SX = single crystal

Table II
Analyzed Compositions (weight percent) of Single Crystal Alloys

Alloy	Al	Cr	Co	Mo	Re	Ta	Y (ppmw)	Ni	B	C	S (ppmw)
LDS-0010	6.1	0.0	0.0	12.0	0.0	6.1	53 top 277 bottom	75.6	0.0040	0.0140	n/a
LDS-0101	6.0	0.0	9.8	7.0	2.9	6.3	70 top 180 bottom	67.9	0.0045	0.0098	n/a
LDS-5051	6.0	2.4	0.0	9.0	3.0	6.1	65 top 174 bottom	73.4	0.0040	0.0140	2.8
LDS-5555	6.0	2.4	4.9	9.5	1.5	6.2	46 top 187 bottom	69.4	0.0032	0.0168	2.8
LDS-1000	6.0	4.8	0.0	7.1	0.0	6.2	48 top 210 bottom	75.8	0.0030	0.0098	3.1
LDS-1101	6.0	4.7	9.9	7.1	3.0	6.2	50 top 193 bottom	63.1	0.0035	0.0160	4.1
LDS-1110	6.0	4.7	9.8	12.0	0.0	6.1	47 top 177 bottom	61.4	0.0030	0.0180	n/a

n/a = not available

Table III
Scale Phases Identified by X-Ray Diffraction
after 200 cycles of 1100°C Cyclic Oxidation

Alloy	Weight (mg/cm^2)	α-Al_2O_3	spinel	spinel, a_0 (Å)	rutile	NiO
LDS-0010	-5.576	W	S	8.060	S	W
LDS-0101	-3.857		S	8.070	S	S
LDS-5051	-0.889	W	M	8.114	S	M
LDS-5555	-0.845		S	8.106	S	S
LDS-1000	0.379	S	S	8.070	S	W
LDS-1110	0.391	S	S	8.070	S	
LDS-1101	0.409	S	S	8.104	S	

where S = strong
M = medium
W = weak

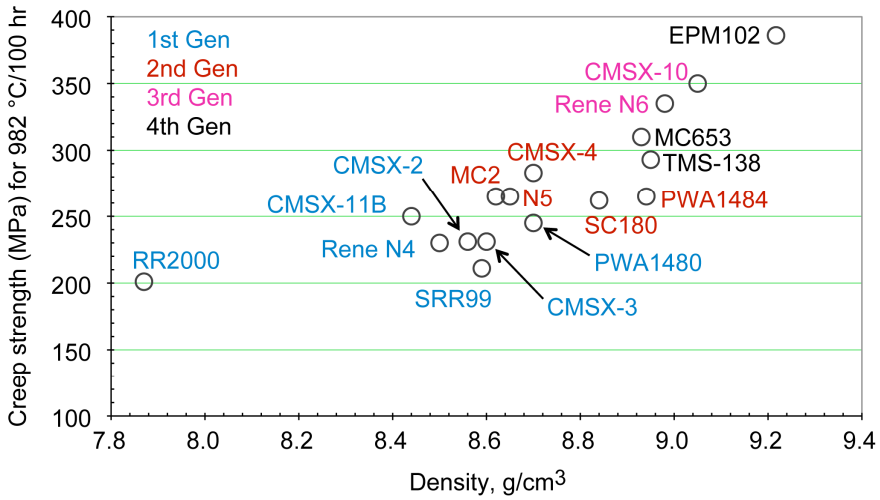

Figure 1.—Single crystal superalloy creep strength has been increased historically along with concurrent increases in alloy density. Data from references 6-8, 10-18.

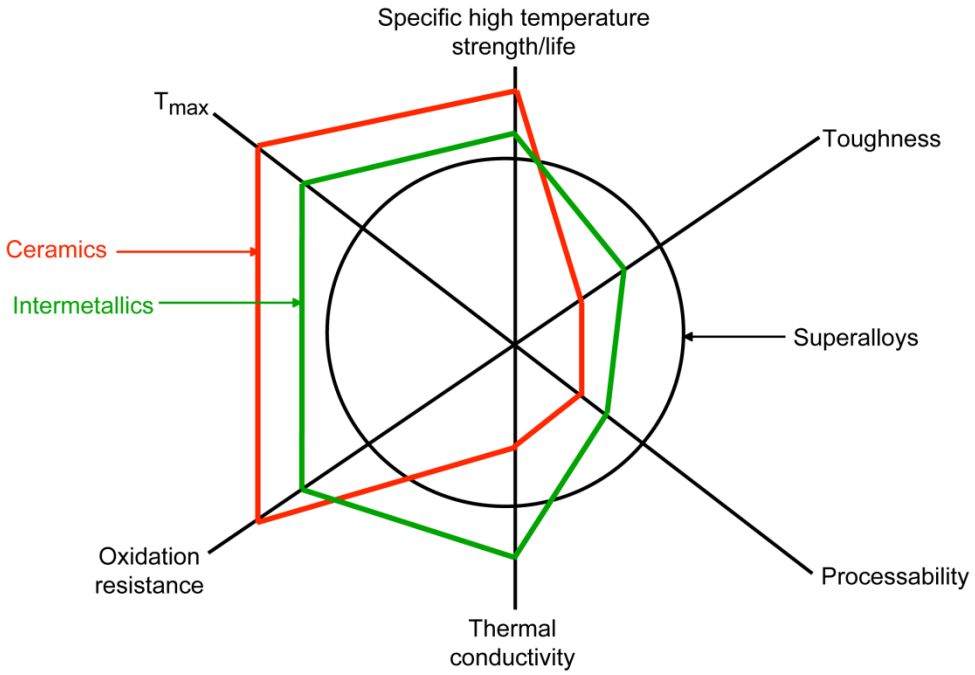

Figure 2.—Comparison of balance of properties required for turbine engine applications. Ceramics and intermetallics are compared to nickel-base superalloys for six different properties.

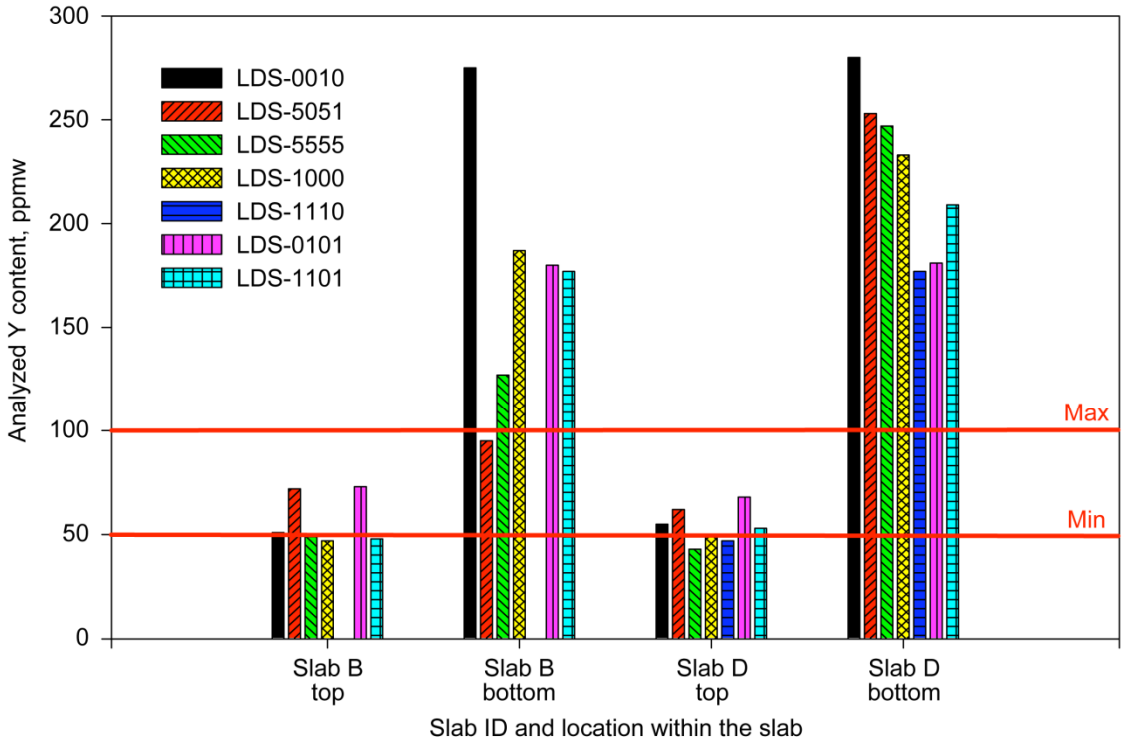

Figure 3.—Analyzed yttrium (Y) contents in the top and bottom sections of two castings of each low density superalloy (LDS). Y contents retained in slab top sections were close to minimum specifications.

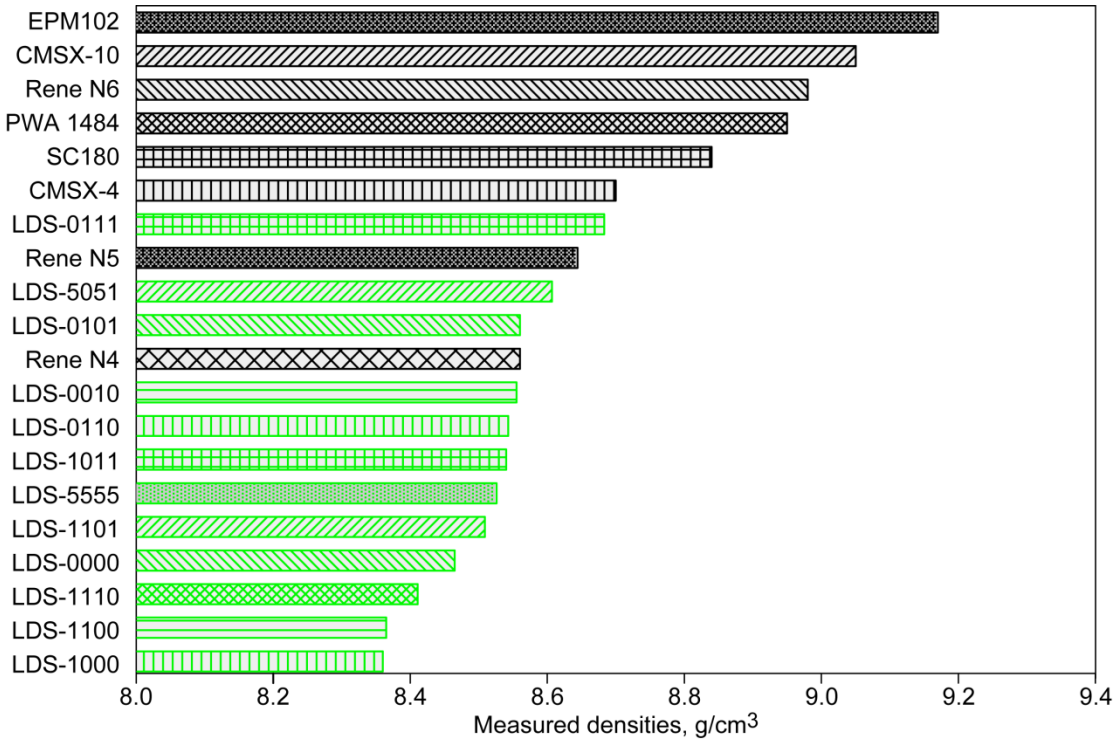

Figure 4.—Measured densities of alloys in LDS design space (in green) are compared to those of first-generation single crystal alloy Rene N4 (8, 9), second-generation single crystal alloys Rene N5 (36), CMSX-4 (7-9), SC180 (7, 8), and PWA 1484 (7-9, 36), third-generation single crystal alloys Rene N6 (8) and CMSX-10 (7-9), and fourth-generation single crystal alloy EPM102 (4).

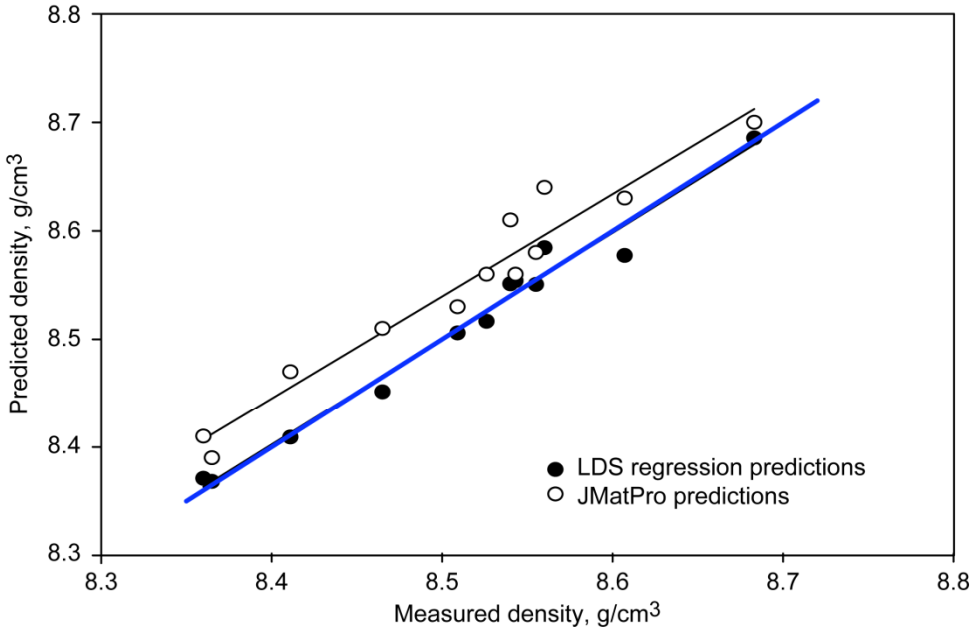

Figure 5.—Good agreement is shown between the alloy densities predicted by the LDS regression model and the measured densities for the alloys cast in the present study. Predictions using JMatPro® 4.0, a software program that utilizes a commercial Ni alloy database, are also shown for comparison. The solid blue line in the figure has a slope of 1.0, indicating that the LDS regression more closely predicted the measured density values.

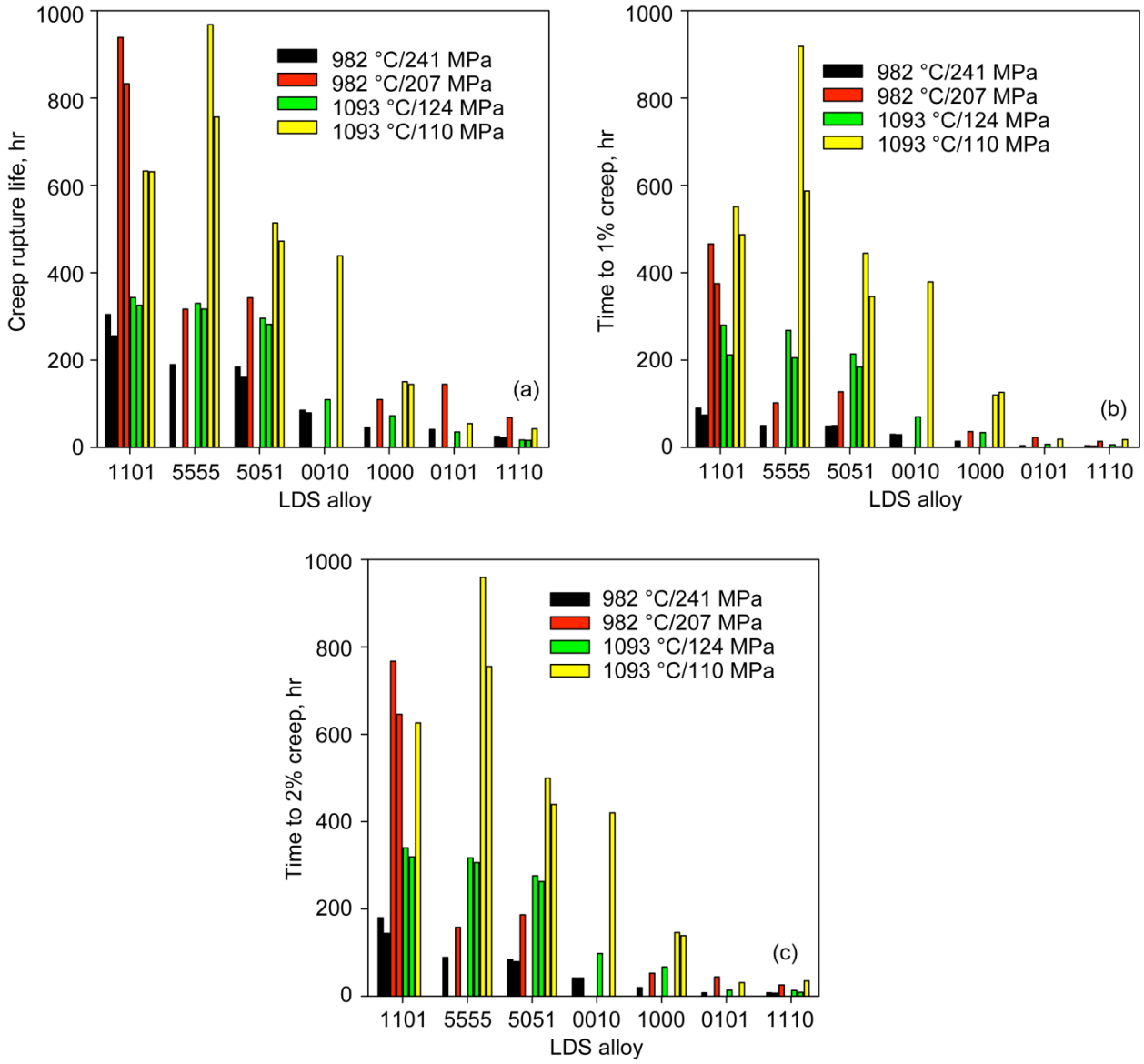

Figure 6.—Creep rupture properties for LDS alloys. (a) Creep rupture life. (b) Time to 1% creep strain. (c) Time to 2% creep strain. Test data are shown for two temperatures and typically two applied stress levels at each temperature.

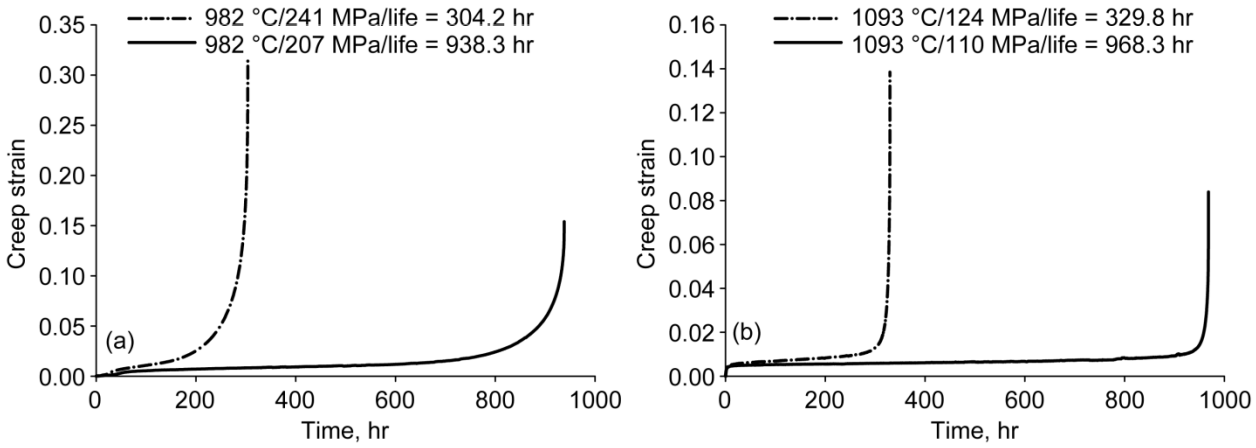

Figure 7.—Typical creep rupture curves for (a) LDS-1101 at 982 °C and (b) LDS-5555 at 1093 °C.

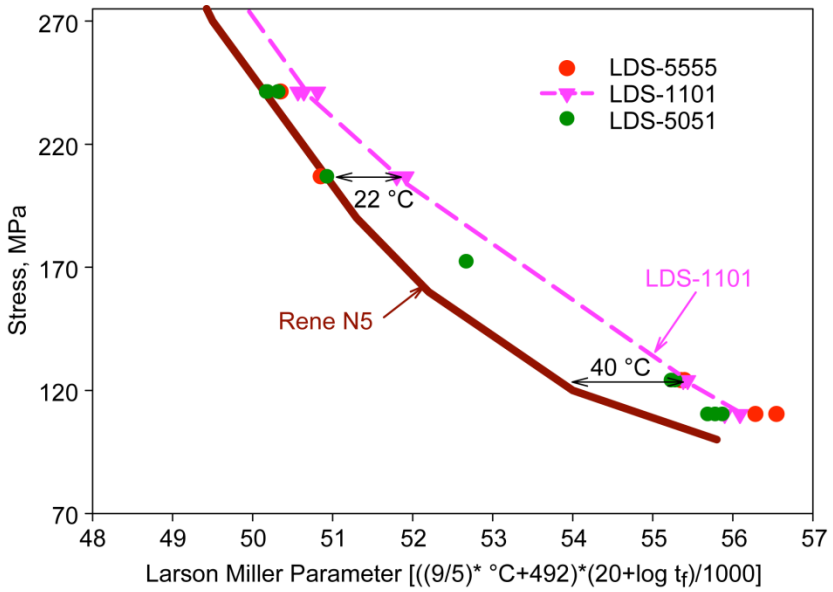

Figure 8.—Larson Miller Parameter plot for three low density single crystal (LDS) superalloys. Comparison to Rene N5 (7) is provided. LDS-1101 has up to a 40 °C temperature advantage over Rene N5.

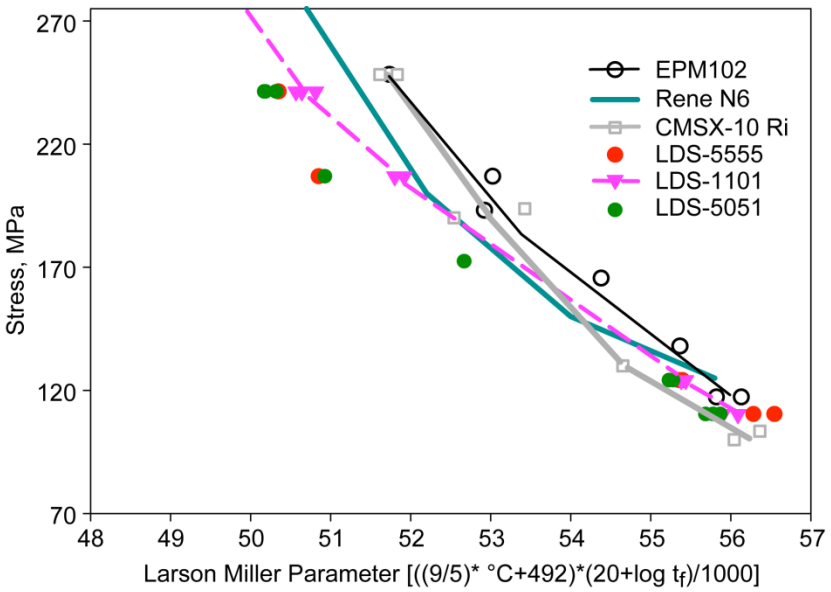

Figure 9.—Larson Miller Parameter plot for three low density single crystal (LDS) superalloys. Comparison to EPM102 (4, 6), Rene N6 (7), and CMSX-10 Ri (38) is provided.

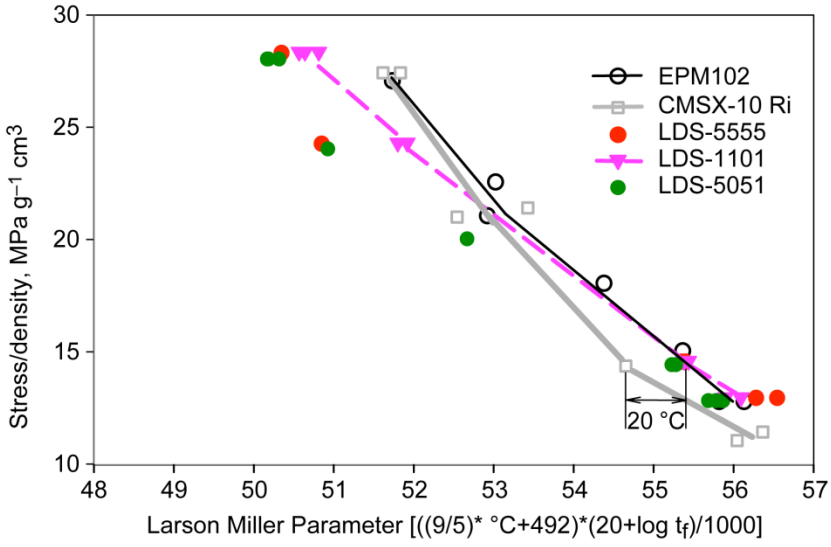

Figure 10.—Larson Miller Parameter plot for three low density single crystal (LDS) superalloys with density normalization made for EPM102 and CMSX-10 Ri. The creep strength data largely collapse when density is taken into account.

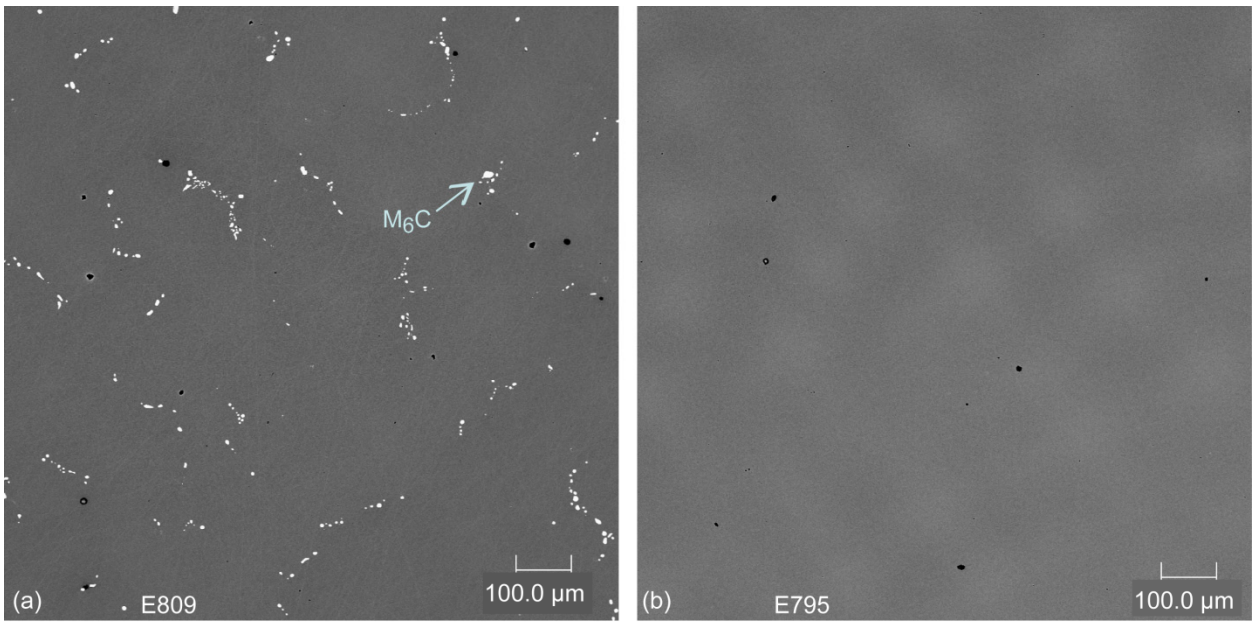

Figure 11.—Typical as-solutioned microstructures in single crystals of (a) LDS-5051 and (b) LDS-1101. LDS-5051 contains carbides in the interdendritic areas, whereas LDS-1101 contains very few carbides after the solutioning treatment. Note that both photos are at the same magnification. Samples are unetched and imaged using back-scattered scanning electron microscopy.

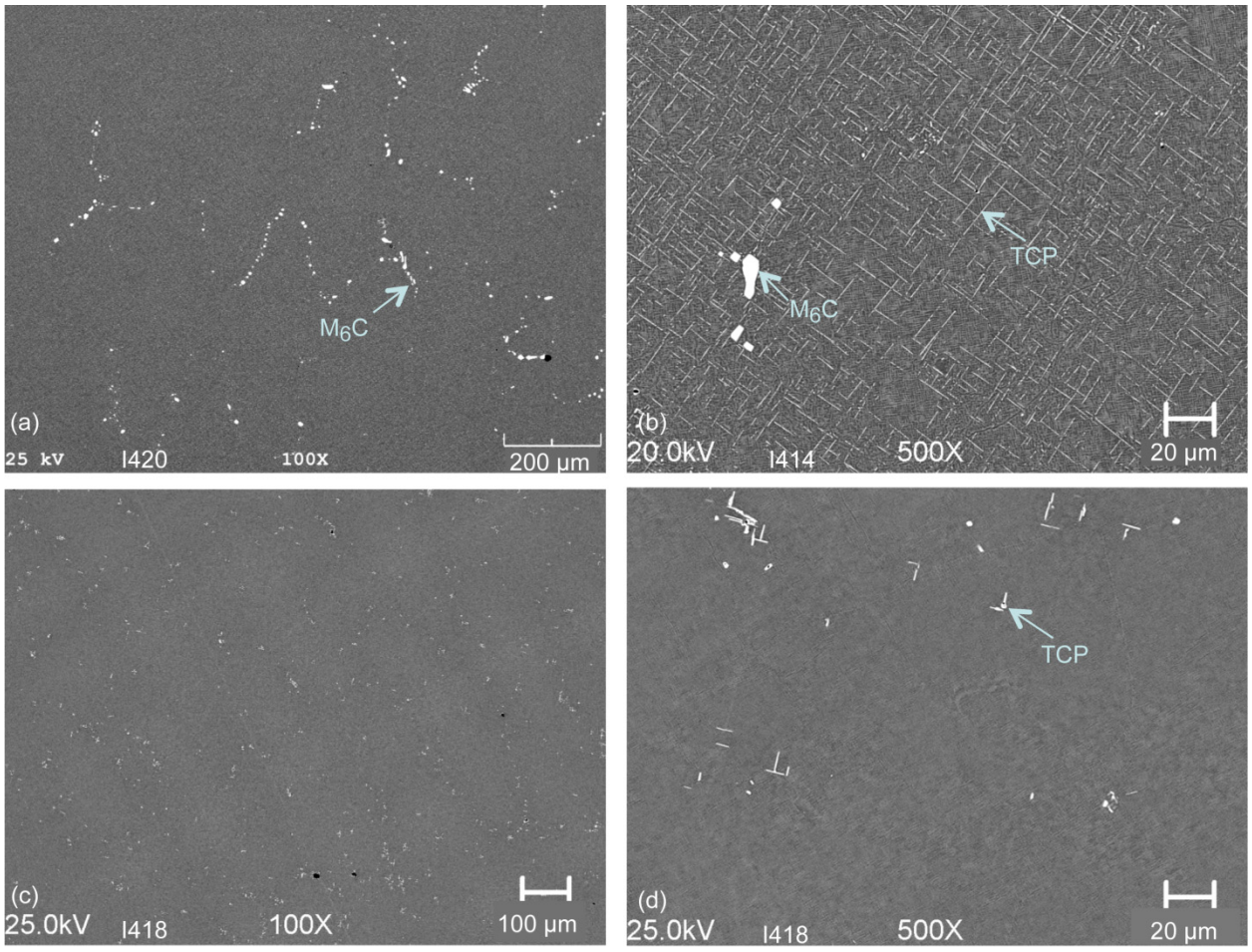

Figure 12.—Microstructures after solution and age at 982 °C for 500 hr in single crystals of (a) LDS-5051 at 100X, (b) LDS-5051 at 500X, (c) LDS-1101 at 100X, and (d) LDS-1101 at 500X. Samples are unetched and imaged using back-scattered scanning electron microscopy.

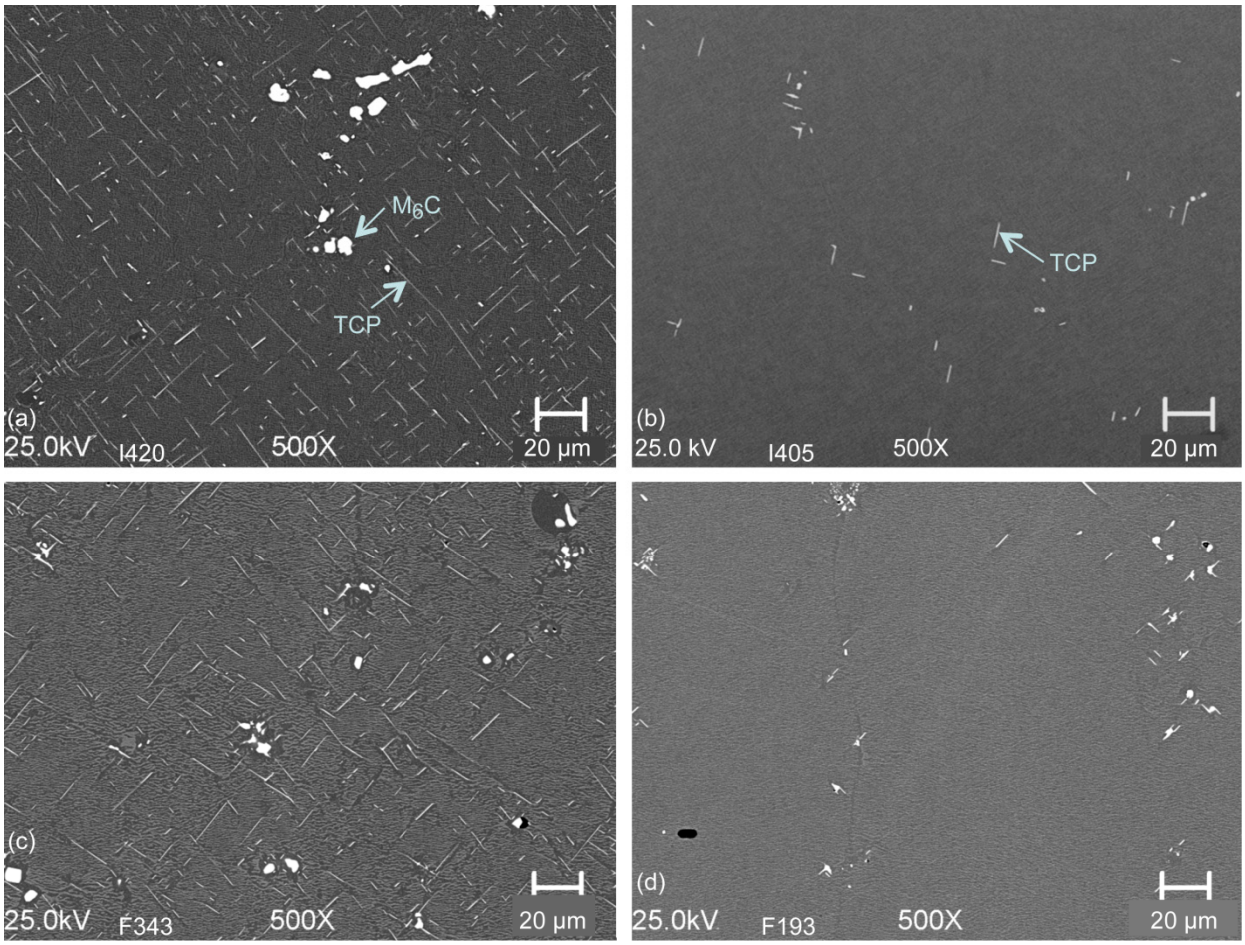

Figure 13.—Microstructures after solution and: (a) aging at 1093 °C for 500 hr in LDS-5051; (b) aging at 1093 °C for 500 hr in LDS-1101; (c) creep testing at 1093 °C at 124 MPa for 296 hr in LDS-5051; and (d) creep testing at 1093 °C at 124 MPa for 343 hr in LDS-1101. Samples are unetched and imaged using back-scattered scanning electron microscopy.

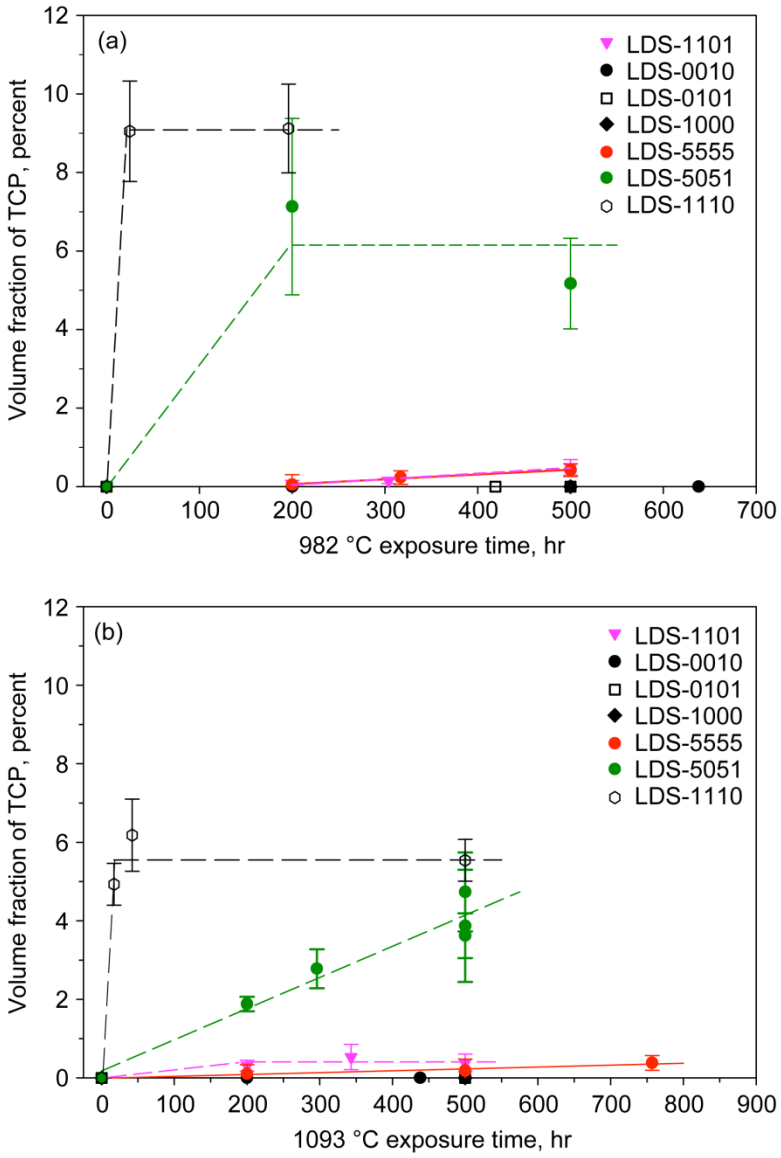

Figure 14.—Volume fraction of Topologically Close Packed (TCP) phase as a function of time for all low density single crystal (LDS) alloys exposed at (a) 982 °C and (b) 1093 °C.

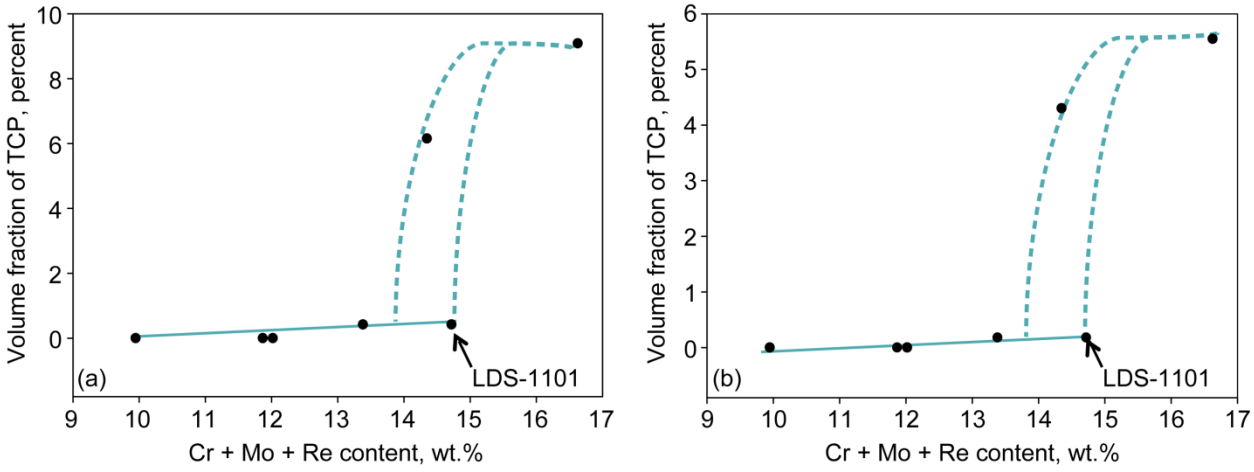

Figure 15.—TCP volume fraction after 500 hr of aging at (a) 982 °C and (b) 1093 °C as a function of analyzed Cr + Mo + Re levels in wt.%.

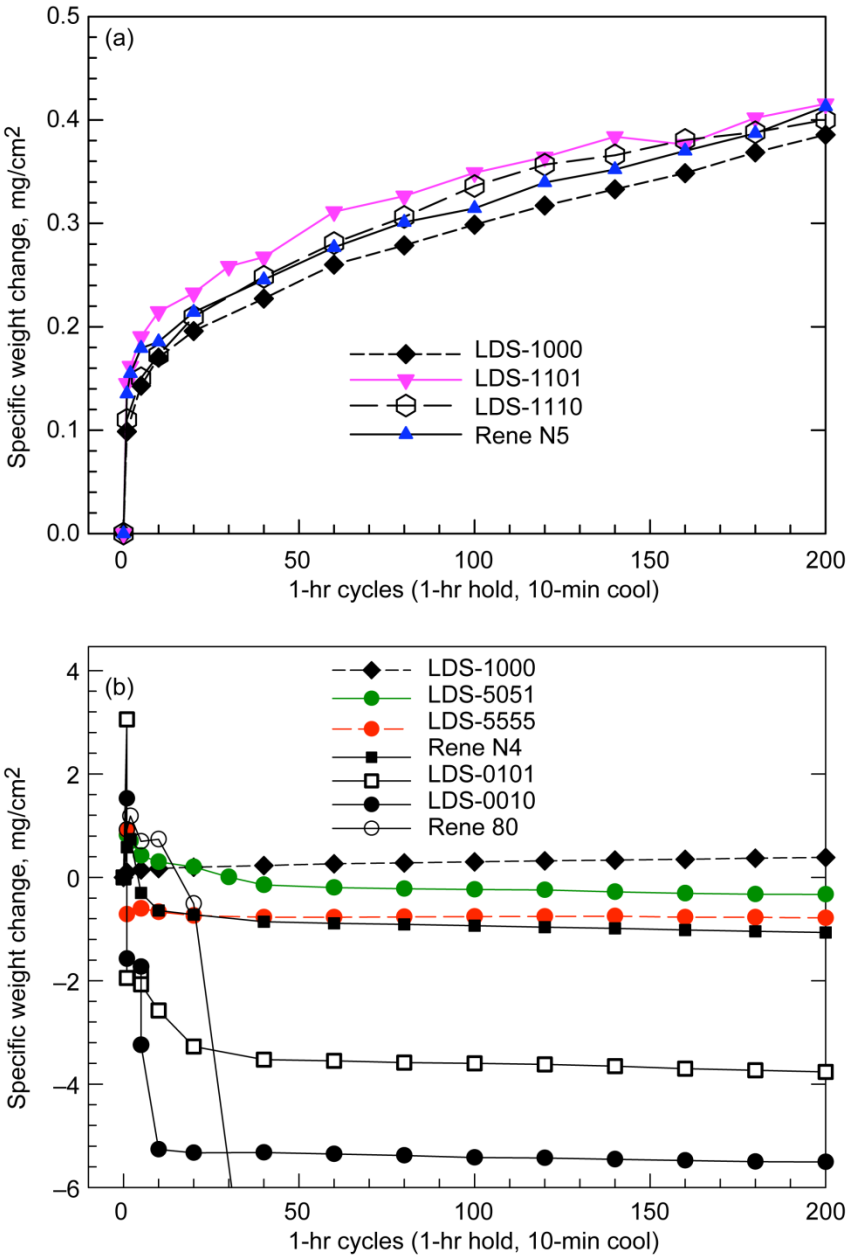

Figure 16.—(a) Similar behavior was exhibited by the 5 wt.% Cr LDS alloys and commercial alloy Rene N5 during 1100 °C cyclic oxidation. (b) LDS alloys and selected commercial alloys (Rene N4 and Rene 80) during 1100 °C cyclic oxidation. An example of an LDS alloy with 5 wt.% Cr (LDS-1000) is shown for comparison to the 2.5 wt.% Cr alloys (LDS-5051 and LDS-5555) and the Cr-free alloys (LDS-0101 and LDS-0010).

(a) (b) (c)

Figure 17.—Cr-bearing (5 wt.%) LDS alloys after 1100 °C cyclic oxidation: (a) LDS-1000, 1 cycle; (b) LDS-1000, 200 cycles; and (c) LDS-1101, 200 cycles. The dominant surface color of the coupons above was termed “gray” in the text; small localized spots of blue oxide may also be seen.

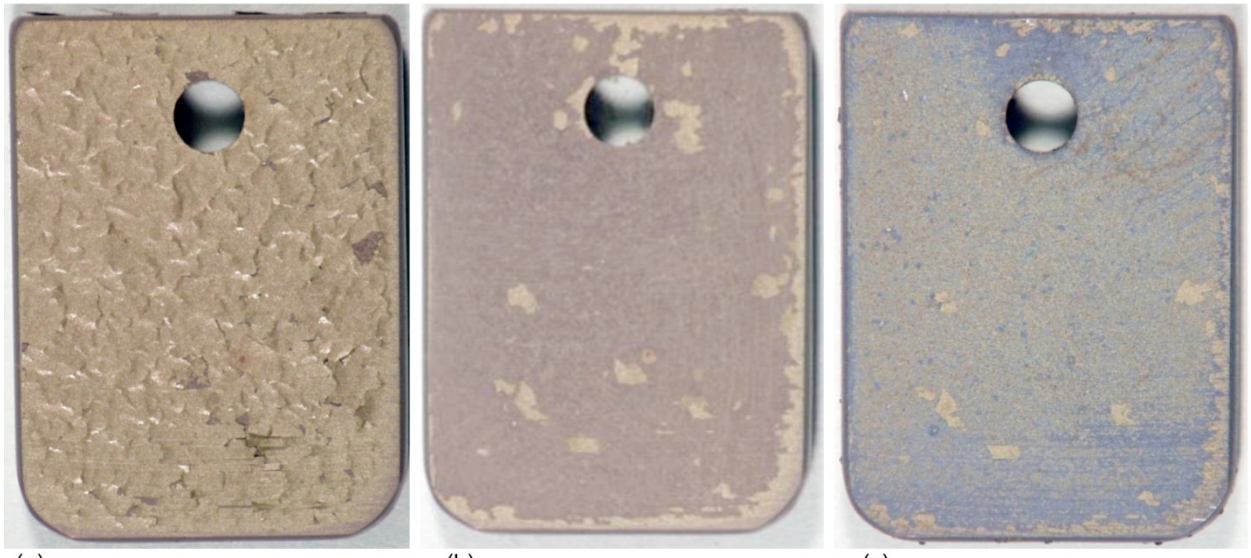

(a) (b) (c)

Figure 18.—LDS-5555 at 2.5 wt.% Cr after 1100 °C cyclic oxidation: (a) as-cycled after 1 cycle; (b) as-brushed after 1 cycle; and (c) as-cycled after 200 cycles.

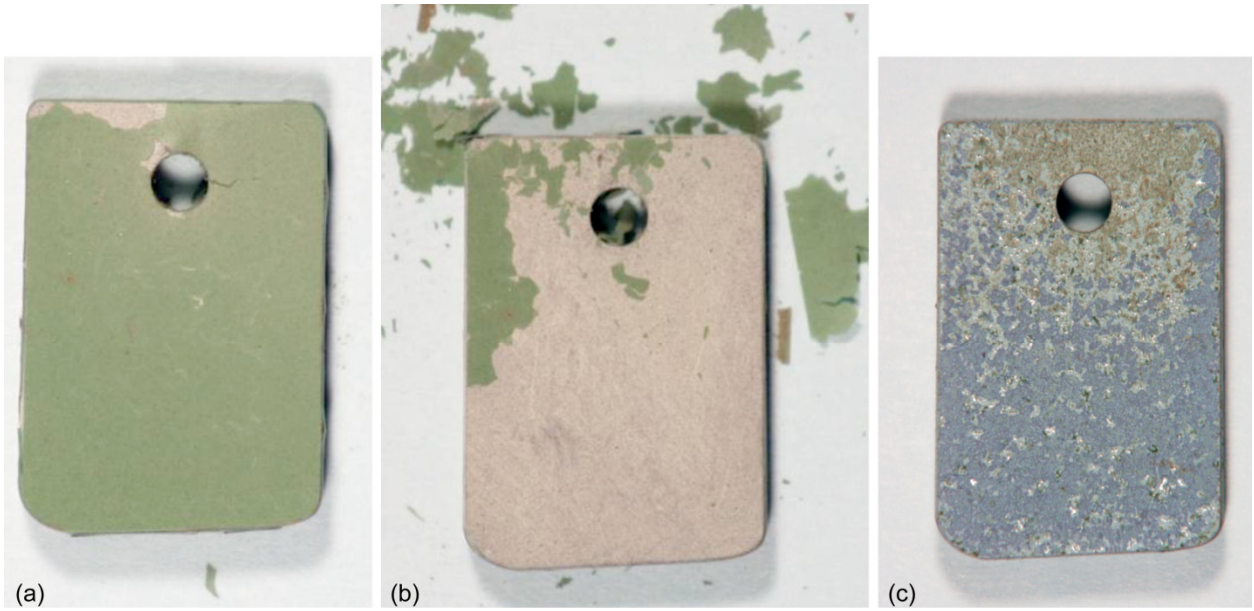

Figure 19.—Cr-free LDS-0010 after 1100 °C cyclic oxidation: (a) as-cycled after 1 cycle; (b) as-brushed after 1 cycle; and (c) as-cycled after 200 cycles.

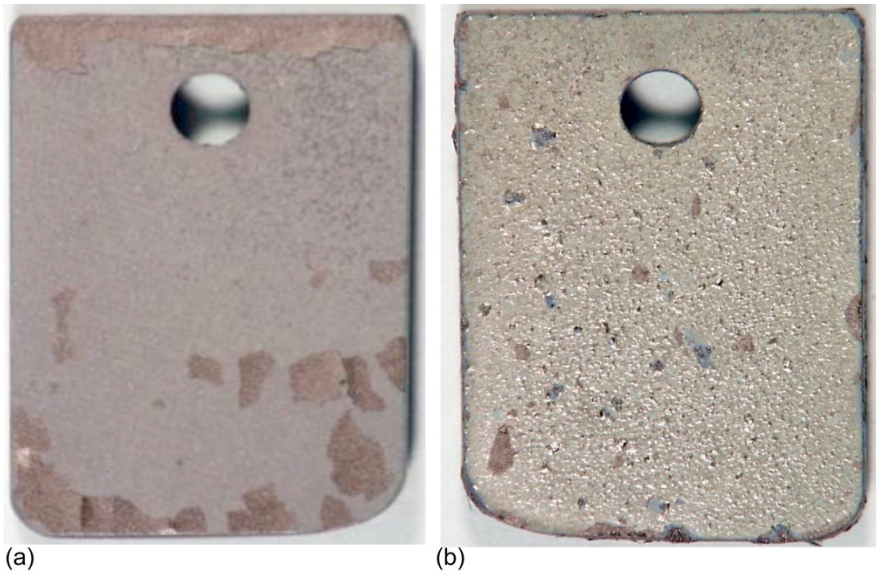

Figure 20.—Cr-free LDS-0101 after 1100 °C cyclic oxidation: (a) as-brushed after 1 cycle; and (b) as-cycled after 200 cycles.

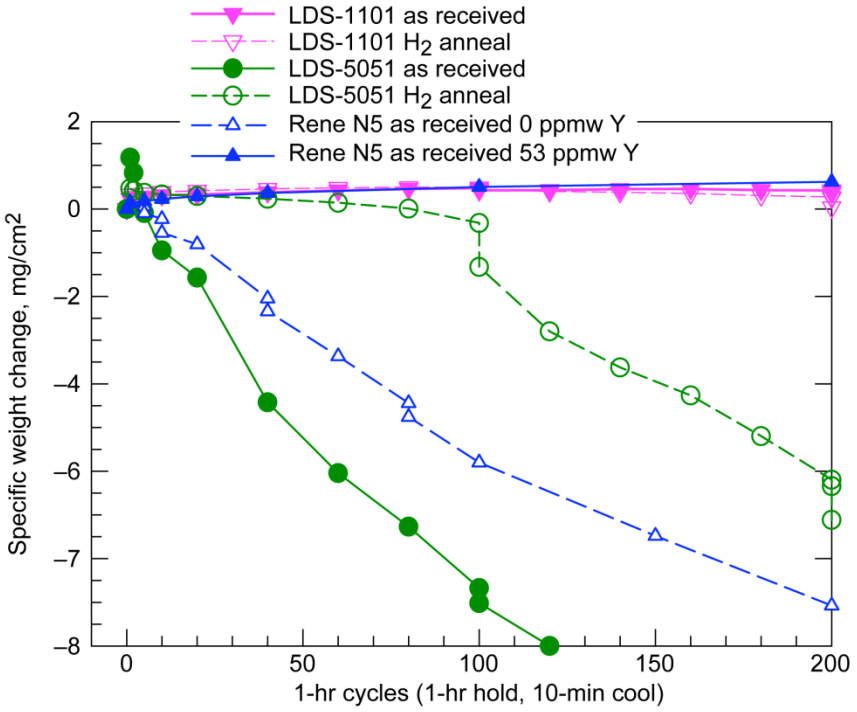

Figure 21.—1150 °C cyclic oxidation data for LDS-1101, LDS-5051, and Rene N5 (with and without Y addition). LDS-1101 looks promising relative to Rene N5. Hydrogen (H_2) annealing was performed on the LDS alloys at 1250 °C/50 hr prior to oxidation testing and was found to improve cyclic oxidation behavior for LDS-5051. Rene N5 data was generated in another cyclic oxidation test and was obtained from Reference 42.

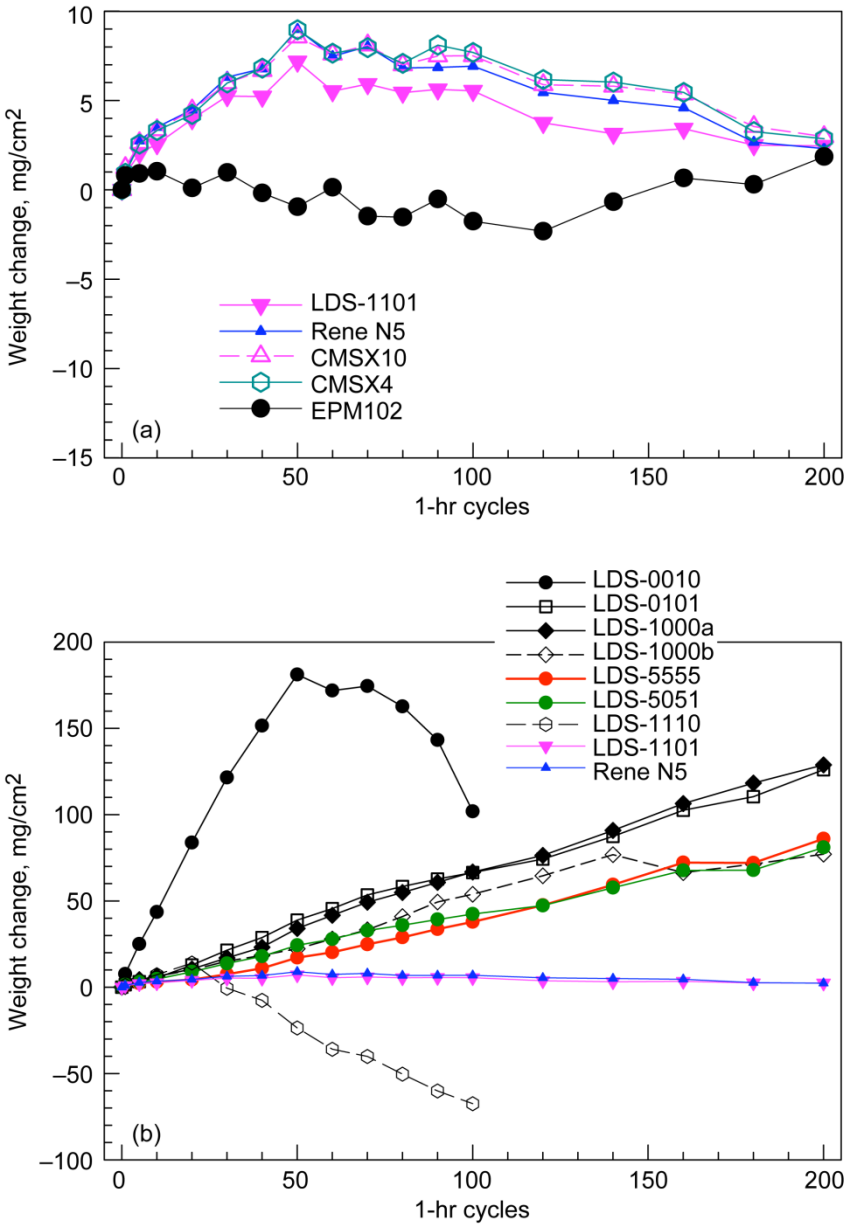

Figure 22.—(a) LDS-1101 follows similar trends in behavior to the commercial alloys shown during testing in Mach 0.3 cyclic hot salt corrosion at 900 °C. Weight change of EPM102 does not follow the pattern of other alloys. (b) A range of behavior is shown for LDS alloys during Mach 0.3 cyclic hot salt corrosion at 900 °C. Selected alloys were stopped after 100 cycles. Note similarity of behavior between LDS-1101 and Rene N5 over 200 cycles of testing.

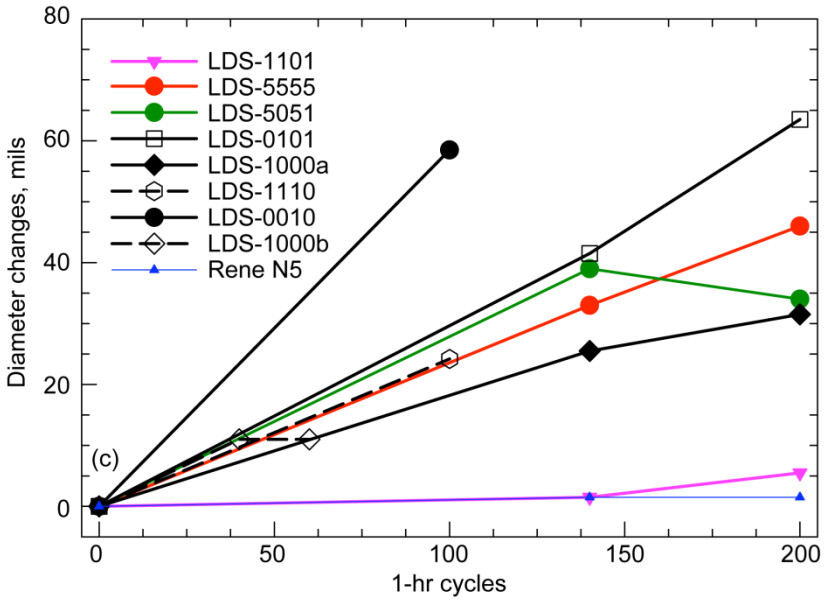

Figure 22.—(c) Maximum pin diameter changes are shown for LDS alloys and Rene N5 during Mach 0.3 cyclic hot salt corrosion at 900 °C. Pin diameter changes were roughly correlated to weight changes. Note similarity of behavior between LDS-1101 and Rene N5 over 200 cycles of testing.

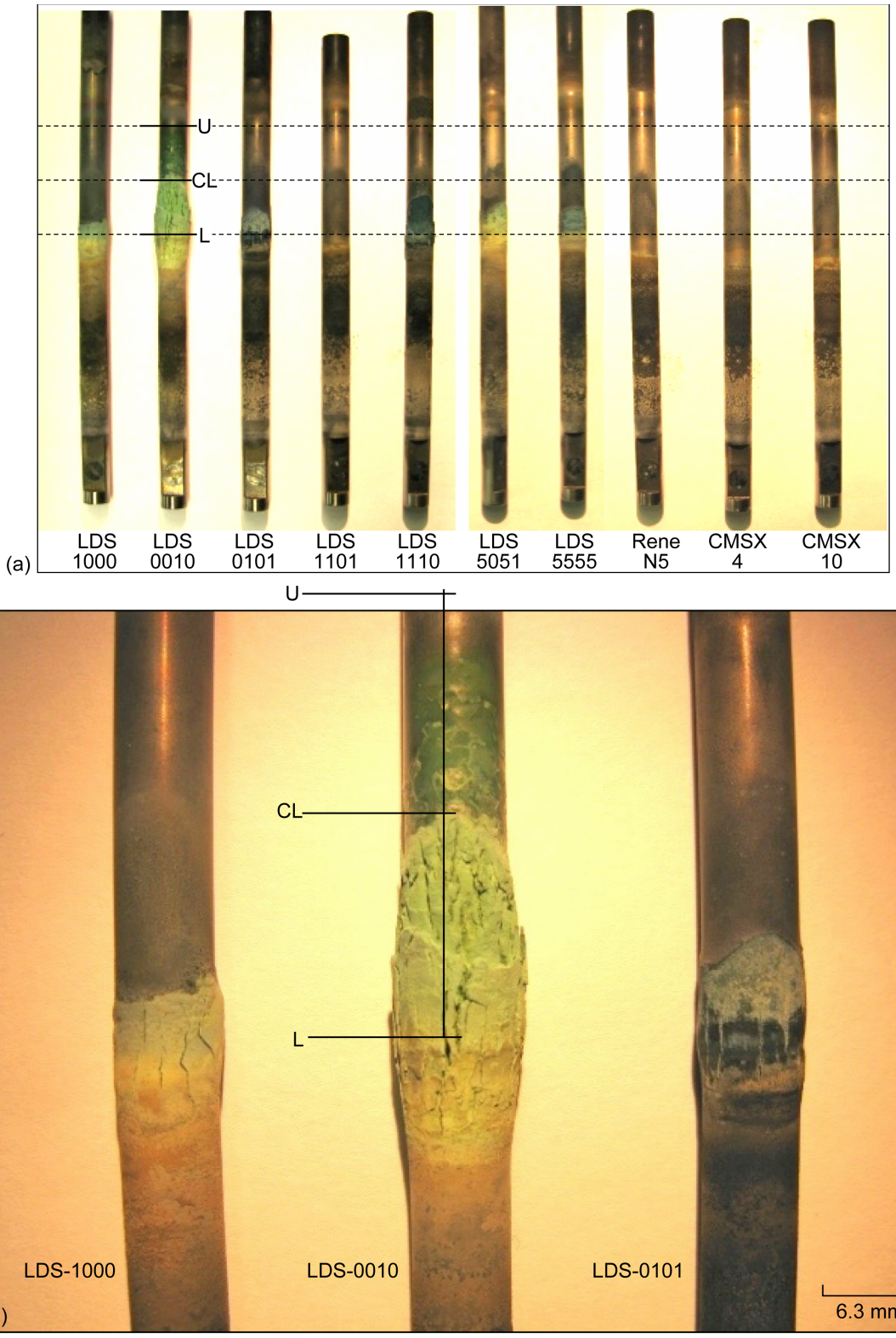

Figure 23.—(a) Macros of pins after 100 cycles of testing in Mach 0.3 hot corrosion at 900 °C, 2 ppm sea salt, and 1-hr cycles. The approximate flame impingement area is indicated on the figure; U and L are the upper and lower extremes, respectively, and CL is the centerline of the flame impingement area. (b) Macros of pins in the burner rig flame impingement area. Maximum corrosion developed below the centerline (CL) of flame impingement. Maximum pin diameter measurements were taken at L in the figure.

REPORT DOCUMENTATION PAGE		Form Approved OMB No. 0704-0188

1. REPORT DATE *(DD-MM-YYYY)*	2. REPORT TYPE	3. DATES COVERED *(From - To)*
01-10-2009	Technical Memorandum	

4. TITLE AND SUBTITLE
Alloy Design Challenge: Development of Low Density Superalloys for Turbine Blade Applications

5a. CONTRACT NUMBER

5b. GRANT NUMBER

5c. PROGRAM ELEMENT NUMBER

6. AUTHOR(S)
MacKay, Rebecca, A.; Gabb, Timothy, P.; Smialek, James, L.; Nathal, Michael, V.

5d. PROJECT NUMBER

5e. TASK NUMBER

5f. WORK UNIT NUMBER
WBS 561581.02.08.03.15.03

7. PERFORMING ORGANIZATION NAME(S) AND ADDRESS(ES)
National Aeronautics and Space Administration
John H. Glenn Research Center at Lewis Field
Cleveland, Ohio 44135-3191

8. PERFORMING ORGANIZATION REPORT NUMBER
E-17081

9. SPONSORING/MONITORING AGENCY NAME(S) AND ADDRESS(ES)
National Aeronautics and Space Administration
Washington, DC 20546-0001

10. SPONSORING/MONITOR'S ACRONYM(S)
NASA

11. SPONSORING/MONITORING REPORT NUMBER
NASA/TM-2009-215819

12. DISTRIBUTION/AVAILABILITY STATEMENT
Unclassified-Unlimited
Subject Category: 26
Available electronically at http://gltrs.grc.nasa.gov
This publication is available from the NASA Center for AeroSpace Information, 443-757-5802

13. SUPPLEMENTARY NOTES

14. ABSTRACT
New low density single crystal (LDS) alloys have been developed for turbine blade applications, which have the potential for significant improvements in the thrust to weight ratio over current production alloys. An innovative alloying strategy was identified to achieve high temperature creep resistance, alloy density reductions, microstructural stability, and cyclic oxidation resistance. The approach relies on the use of molybdenum (Mo) as a potent solid solution strengthener for the nickel (Ni)-base superalloy; Mo has a density much closer to Ni than other refractory elements, such as rhenium (Re) or tungsten (W). A host of testing and microstructural examinations was conducted on the superalloy single crystals, including creep rupture testing, microstructural stability, cyclic oxidation, and hot corrosion. The paper will provide an overview of the single crystal properties that were generated in this new superalloy design space. The paper will also demonstrate the feasibility of this innovative approach of low density single crystal superalloy design. It will be shown that the best LDS alloy possesses the best attributes of three generations of single crystal alloys: the low density of first-generation single crystal alloys, the excellent oxidation resistance of second-generation single crystal alloys, and a creep strength which exceeds that of second and third generation alloys.

15. SUBJECT TERMS
Superalloy; Heat resistant alloy; Single crystal; Mechanical properties; Physical properties; Density; Creep properties; Creep-rupture; Oxidation; Hot corrosion; Nickel

16. SECURITY CLASSIFICATION OF:			17. LIMITATION OF ABSTRACT	18. NUMBER OF PAGES	19a. NAME OF RESPONSIBLE PERSON
a. REPORT	b. ABSTRACT	c. THIS PAGE			STI Help Desk (email:help@sti.nasa.gov)
U	U	U	UU	45	19b. TELEPHONE NUMBER *(include area code)* 443-757-5802